

Molecular Outflows in W5

Adam Ginsburg^{1*}, John Bally¹, and Jonathan P. Williams²

¹Center for Astrophysics and Space Astronomy, University of Colorado 389 UCB, Boulder, CO 80309-0389

²Institute for Astronomy University of Hawaii 2680 Woodlawn Dr. Honolulu, HI 96822

28 October 2010

ABSTRACT

New JCMT HARP CO 3-2 observations of the W5 star forming complex are presented, totaling an area of ~ 12000 arcmin² with sensitivity better than 0.1 K per 0.4 km s⁻¹ channel. 55 CO outflows have been discovered, 40 of which are associated with W5. Most of the outflows are located on the periphery of the W5 HII region, but two clusters of outflows are > 5 pc from the ionization fronts, indicating that they have formed stars without directly being triggered by the O-stars in W5. We have compared the derived outflow properties to those in Perseus and find that the W5 outflow masses are surprisingly low. The outflow deficiency in this more massive ($M \sim 6.5 \times 10^4 M_\odot$) cloud can be explained if ionizing radiation destroys many of the molecular outflows, rendering them undetectable. It is noted that CO 3-2, while a good tracer of outflows, may be a poor mass tracer because of sub-thermal line excitation. Despite the caveat that much outflowing mass is not observed, it is unlikely that outflows can provide the observed turbulent energy in the W5 molecular clouds. Many cometary globules have been observed with velocity gradients from head to tail and therefore show strong interaction with the W5 HII region. Because it is observed face-on in a sheet-like geometry, W5 is an excellent region to study the feedback effects, both positive and negative, of massive stars on star formation.

Key words: ISM: jets and outflows — ISM: kinematics and dynamics — ISM: individual: W5 — stars: formation

1 INTRODUCTION

Galactic-scale shocks such as spiral density waves promote the formation of giant molecular clouds (GMCs) where massive stars, star clusters, and OB associations form. The massive stars in such groups can either disrupt the surrounding medium or promote further star formation. While ionizing and soft UV radiation, stellar winds, and eventually supernova explosions destroy clouds in the immediate vicinity of massive stars, as the resulting bubbles age and decelerate, they can also trigger further star formation. In the “collect and collapse” scenario (e.g. Elmegreen & Lada 1977), gas swept-up by expanding bubbles can collapse into new star-forming clouds. In the “radiation-driven implosion” model (Bertoldi & McKee 1990; Klein et al. 1983), pre-existing clouds may be compressed by photo-ablation pressure or by the increased pressure as they are overrun by an expanding shell. In some circumstances, forming stars are simply exposed as low-density gas is removed by the action of massive stars. These processes may play significant roles in determin-

ing the efficiency of star formation in clustered environments (Elmegreen 1998).

Feedback from low mass stars may also control the shape of the stellar initial mass function in clusters (Adams & Fatuzzo 1996; Peters et al. 2010). Low mass young stars generate high velocity, collimated outflows that contribute to the turbulent support of a gas clump, preventing the clump from forming stars before it is blown away by massive star feedback. It is therefore important to understand the strength of low-mass protostellar feedback.

Outflows are a ubiquitous indicator of the presence of ongoing star formation (Reipurth & Bally 2001). CO outflows are an indicator of ongoing embedded star formation at a younger stage than optical outflows because shielding from the interstellar radiation field is required for CO to survive. Although Herbig-Haro shocks and H₂ knots reveal the locations of the highest-velocity segments of these outflows, CO has typically been thought of as a “calorimeter” measuring the majority of the mass and momentum ejected from protostars or swept up by the ejecta (Bachiller 1996).

* adam.ginsburg@colorado.edu

1.1 W5

The W5 star forming complex in the outer galaxy is a prime location to study massive star formation and triggering. The bright-rimmed clouds in W5 have been recognized as good candidates for ongoing triggering by a number of groups (Lefloch et al. 1997; Thompson et al. 2004; Karr & Martin 2003). The clustering properties were analyzed by Koenig et al. (2008) using Spitzer infrared data, and a number of significant clusters were discovered. The whole W5 complex may be a product of triggering, as it is located on one side of the W4 chimney thought to be created by multiple supernovae during the last ~ 10 MYr (Oey et al. 2005, Figure 1).

Following Koenig et al. (2008), we adopt a distance to W5 of 2 kpc based on the water-maser parallax distance to the neighboring W3(OH) region (Hachisuka et al. 2006). As with W3, the W5 cloud is substantially ($\approx 1.5 \times$) closer than its kinematic distance would suggest ($v_{LSR}(-40 \text{ km s}^{-1}) \approx 3 \text{ kpc}$).

The W5 complex was mapped in the ^{12}CO 1-0 emission line by the FCRAO using the SEQUOIA receiver array (Heyer et al. 1998). The same array was used to map W5 in the ^{13}CO 1-0 line (C. Brunt, private communication). Some early work was done to search for outflows in W5 (Bretherton et al. 2002), but the low-resolution CO 1-0 data only showed a few (and only one was published). Higher excitation lines are better suited to the discovery of outflows because outflows tend to have low beam filling factors but high excitation temperatures, and they stand out better against the lower background in higher energy transitions.

2 OBSERVATIONS

2.1 JCMT HARP-B CO 3-2

CO J=3-2 345.79599 GHz data were acquired at the 15m James Clerk Maxwell Telescope (JCMT) using the HARP-B array on a series of observing runs in 2008 and 2009. On 2-4 January, 2008, ~ 800 square arcminutes were mapped with a beam size $\sim 12''$. During the run, τ_{225} ranged from 0.1 to 0.4. Additional areas were mapped on 4-7 August, 16-20 and 31 October, and 1 and 12-15 Nov in similar conditions. A total of ~ 3 square degrees (12000 arcmin^2) in the W5 complex were mapped (a velocity-integrated mosaic is shown in Figure 2).

HARP-B is a 16 pixel SIS receiver array acting as a front-end to the ACSIS digital auto-correlation spectrometer. In January 2008, 14 of the 16 detectors were functional. In the 2nd half of 2008, 12 of 16 were functional, necessitating longer scans to achieve similar S/N.

In 2008, a single spectral window centered at 345.7959899 with bandwidth 1.0 GHz and channel width 488 kHz (0.42 km s^{-1}) was used. In 2009, two spectral windows centered at 345.7959899 and 346.99854 GHz (CO 3-2 and $^{13}\text{HCO}^+$ 4-3) with bandwidth 250 MHz and channel width 61 kHz (0.05 km s^{-1}) were used. Only the CO 3-2 data are presented here. At these frequencies, the beam FWHM is $14''$ (0.14 pc at a distance of 2 kpc).

A raster mapping strategy was used. In 2008, the array was shifted by 1/2 of a receptor spacing ($7''$) between scans. Data was sampled at a rate of 1.67 s^{-1} . Two perpendicular

scans were used for each patch observed. Most patches were $10 \times 10'$ and took ~ 45 minutes. When only 12 receptors were available, 1/4 array stepping was used with a sample rate of 2.5 s^{-1} .

Data were reduced using the STARLINK package. MAKECUBE was used to generate mosaics of contiguous sub-fields. The data were gridded on to cubes with $6''$ pixels and smoothed with a $\sigma = 2$ -pixel gaussian, resulting in a map FWHM resolution of $18''$ (0.17 pc). A linear fit was subtracted from each spectrum over emission-free velocities (generally -60 to -50 and -20 to -10 km s^{-1}) to remove the baseline. The final map RMS was $\sigma_{T_A^*} \sim 0.06 - 0.11 K$ in 0.42 km s^{-1} channels.

The sky reference (off position) in 2008 was J2000 2:31:04.069 +62:59:13.81. In later epochs, different off positions selected from blank sky regions identified in early 2008 were used to increase observing efficiency. A main-beam efficiency $\eta_{mb} = 0.60$ was used as per the JCMT website to convert measurements to T_{mb} , though maps and spectra are presented in the original T_A^* units.

2.2 FCRAO OGS

The Five College Radio Astronomy Observatory (FCRAO) Outer Galaxy Survey (OGS) observed the W5 complex in ^{12}CO (Heyer et al. 1998) and ^{13}CO 1-0 (C. Brunt, private communication). The ^{13}CO data cube achieved a mean sensitivity of 0.35 K per 0.13 km s^{-1} channel, or 0.6 K km s^{-1} integrated. The ^{13}CO cube was integrated over all velocities and resampled to match the BGPS map using the MONTAGE¹ package. The FWHM beam size was $\theta_B = 50''$ (0.48 pc).

2.3 Spitzer

Spitzer IRAC and MIPS $24 \mu\text{m}$ images from Koenig et al. (2008) were used for morphological comparison. The reduction and extraction techniques are detailed in their paper.

3 ANALYSIS

3.1 Outflow Detections

Outflows were identified in the CO data cube by searching through position-velocity space for line wings using STARLINK's GAIA. Outflow candidates were identified by high velocity wings inconsistent with the local cloud velocity distribution, which ranged from a width of 3 km s^{-1} to 7 km s^{-1} . Once an outflow candidate was identified in the position-velocity diagrams, the velocity range over which the wing showed emission in the position-velocity diagram (down to $T_A^* = 0$) was integrated over to create a map from which the approximate outflow size and position was determined (e.g. Figure 3).

Unlike Curtis et al. (2010) and Hatchell & Dunham (2009), we did not use an 'objective' outflow identification because of the greater velocity complexity and poorer spatial resolution of our observations. As shown in Figure 11, the regions associated with outflows have wide lines and many are

¹ <http://montage.ipac.caltech.edu/>

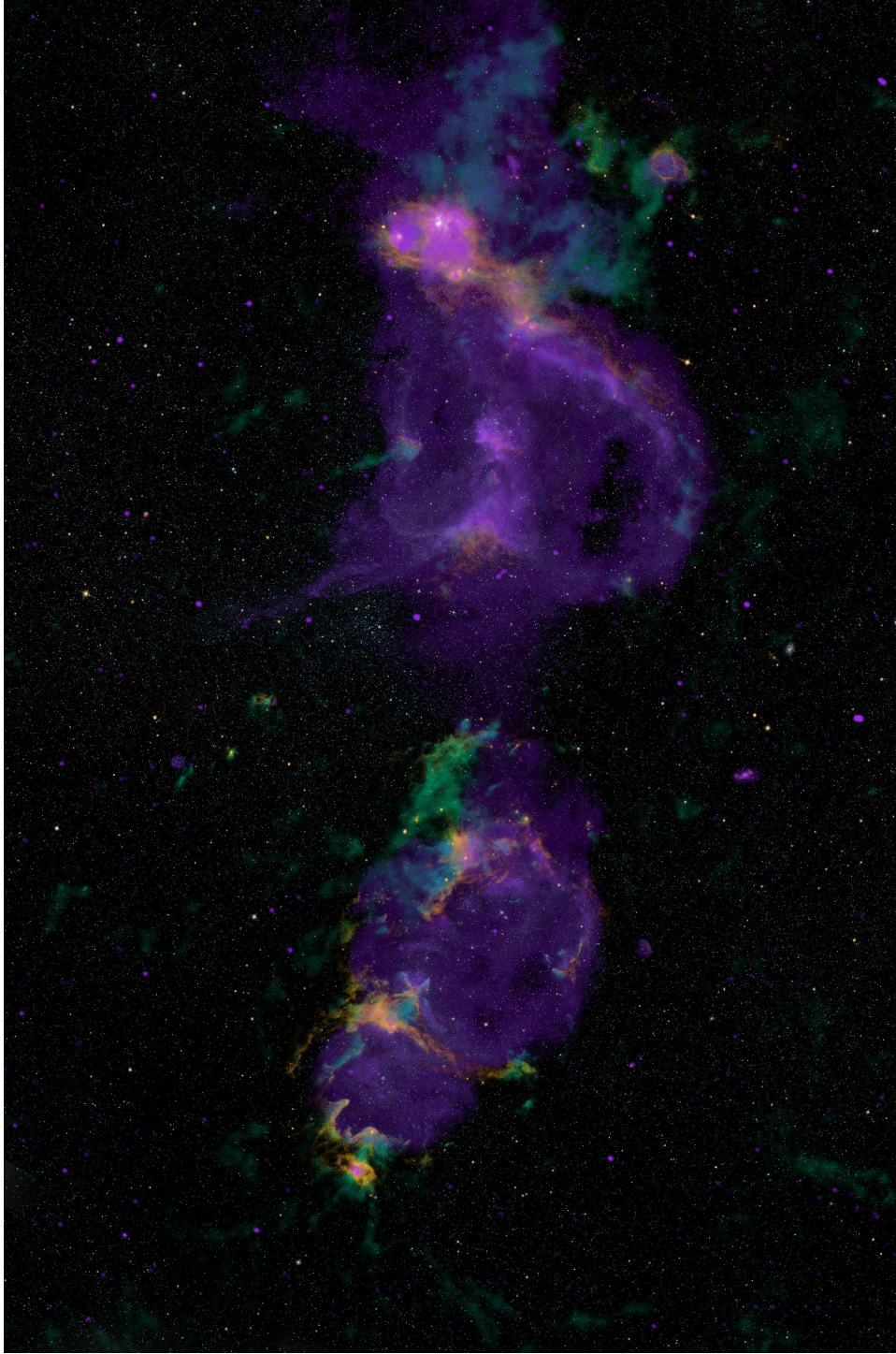


Figure 1. An overview of the W3/4/5 complex (also known as the “Heart and Soul Nebula”) in false color. Orange shows $8 \mu\text{m}$ emission from the Spitzer and MSX satellites. Purple shows 21 cm continuum emission from the DRAO CGPS (Taylor et al. 2003); the DSS R image was used to set the display opacity of the 21 cm continuum as displayed (purely for aesthetic purposes). The green shows FCRAO ^{12}CO 1-0 and JCMT ^{12}CO 3-2. The image spans $\sim 7^\circ$ in galactic longitude. This overview image shows the hypothesized interaction between the W4 superbubble and the W3 and W5 star-forming regions (Oey et al. 2005).

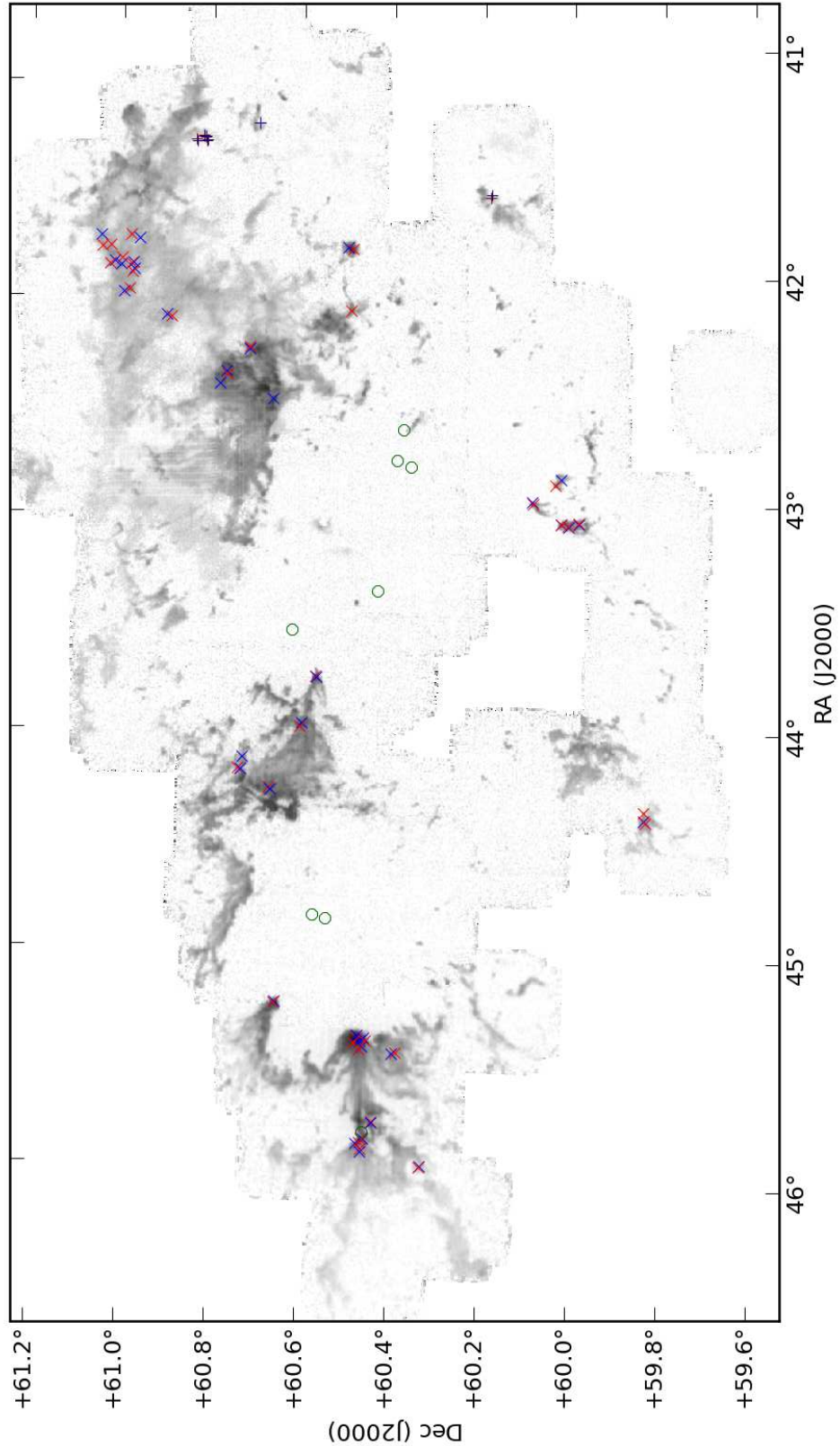


Figure 2. A mosaic of the CO 3-2 data cube integrated from -20 to -60 km s⁻¹. The grayscale is linear from 0 to 150 K km s⁻¹. The red and blue X's mark the locations of redshifted and blueshifted outflows. Dark red and dark blue plus symbols mark outflows at outer arm velocities. Green circles mark the location of all known B0 and earlier stars in the W5 region from SIMBAD.

double-peaked. Additionally, many smaller areas associated with outflows have collections of gaussian-profiled clumps that are not tied to the cloud in position-velocity diagrams but are not outflows. In particular, W5 is pockmarked by many dozens of small cometary globules that are sometimes spatially coincident with the clouds but slightly offset in velocity.

While Arce et al. (2010) has described the benefits of 3D visualization using isosurface contours, we found that the varying signal-to-noise across large-scale ($\sim 500 \text{ pixel}^2$) regions with significant extent in RA/Dec and very limited velocity dynamic range made this method difficult for W5. There were many low-intensity outflows that were detectable by careful searches through position-velocity space that are not detectable via isosurface methods.

In the majority of sources, the individual lobes of the outflows were unresolved, although some showed hints of position-velocity gradients at low significance and in many the red and blue flows are spatially distinct. The most suggestive gradients occurred where the outflow merged with its host molecular cloud in position-velocity space, making the gradient difficult to distinguish. Only Outflow 1's lobes were clearly resolved (Figure 4). Bipolar pairs were selected when there were red and blue flows very nearby one another. The AFGL 4029 region has many red and blue outflows but confusion prevented pairing.

In cases where only the red- or blue-shifted outflow was visible, the surrounding pixels were searched for lower-significance and velocity counterparts. In cases in which significant emission was detected, a candidate counterflow was identified and incorporated into the catalog. However, in 12 cases, the counter flow still evaded detection.

The outflow positions are overlaid on the CO 3-2 image in Figure 2 to provide an overview of where star formation is most active. The figures in Section 4.2 show outflow locations overlaid on small-scale images.

Because our detection method involved searching for high-velocity outflows directly by eye, there should be no false detections. However, it is possible that some of the identified outflows are generated by mechanisms other than standard low-mass protostellar outflows since we have not found the driving sources of these flows.

3.1.1 Comparison to Perseus CO 3-2 observations

We used the HARP CO 3-2 cubes from Hatchell et al. (2007) to evaluate our ability to identify outflows. We selected the most powerful outflow that was well-resolved and unconfused, L1448, and evaluated it at both the native sensitivity of the Hatchell et al. (2007) observations and degraded in resolution and sensitivity to match our own. In particular, we examine L1448 IRS2, labeled Outflow 30 in Hatchell et al. (2007). Figure 5 shows a comparison between the original quality and degraded data.

By integrating over the outflow velocity range, we measure each lobe to be about $1.6' \times 0.8'$ ($0.14 \times 0.07 \text{ pc}$). Assuming a distance to Perseus of 250 pc (in keeping with much of the literature, e.g. Enoch et al. 2006), we smooth by a factor of 8 by convolving the data cube with a FWHM = $111''$ gaussian. The resulting noise in this image is $\approx 0.05 \text{ K}$ per 0.54 km s^{-1} channel, which is comparable to the sensitivity in our survey. It is still possible to distinguish the outflows

from the cloud in position-velocity space. Each lobe is individually unresolved (long axis $\sim 12''$ compared to our beam FWHM of $18''$), but the two are separated by $\gtrsim 20''$ and therefore an overall spatial separation can still be measured. Because they are just barely unresolved at this distance, the lobes' surface brightnesses are approximately the same at 2 kpc as at 250 pc; if this outflow were seen at a greater distance it would appear fainter.

Hatchell et al. (2007) detected 4 outflows within this map, plus an additional confused candidate. We note an additional grouping of outflowing material in the north-middle of the map (centered on coordinate 150×150 in Figure 5). In the smoothed version, only three outflows are detected in the blue and two in the red, making flow-counterflow association difficult. The north-central blueshifted component appears to be the counterpart of the red flow when smoothed, although it is clearly the counterpart of the northwest blue flow in the full-resolution image.

We are therefore able to detect any outflows comparable to L1448 (assuming a favorable geometry), but are likely to see clustered outflows as single or possibly extended lobes and will count fewer flows than would be detected at higher resolution. Additionally, it is clear from this example that two adjacent outflows with opposite polarity are not necessarily associated, and therefore the outflows' source(s) may not be between the two lobes.

In order to determine overall detectability of outflows compared to Perseus, we compare to Curtis et al. (2010). Out of 29 outflows in their survey with measured 'lobe lengths', 22 (71%) were smaller than $128''$ which would be below our $18''$ resolution when smoothed to W5's distance. Even the largest outflow lobes (HRF26R, HRF28R, HRF44B) would only extend $\sim 60''$ at 2 kpc. Each lobe in the largest outflow in our survey, Outflow 1, is $\sim 80''$ (660 '' at 250pc), but no other outflows in W5 are clearly resolved.

Curtis et al. (2010) outflow velocities are similar on average to ours (Figure 6). We detect lower velocity outflows because we do not set a strict lower-limit criterion. We do not detect the highest velocity outflows most likely because of our poorer sensitivity to the faint high-velocity tips of outflows.

3.1.2 Measurements

The measured outflow properties and source associations are presented in Table 2. The outflow velocity ranges were measured by examining both RA-velocity and Dec-velocity diagrams interactively using the STARLINK GAIA data cube viewing tool. The outflow velocity limits are set to include all outflow emission that is distinguishable from the cloud (i.e. the velocity at which outflow emission visibly dominates over the gaussian wing of the cloud emission) down to zero emission. An outflow size (or lobe size, following Curtis et al. 2010) was determined by integrating over the blue and red velocity ranges and creating an elliptical aperture to include both peaks (the integrated outflow maps are shown as red and blue contours in Figure 3); the position and size therefore have approximately beam-sized ($\approx 18''$) accuracy. The velocity center was computed by fitting a gaussian to the ^{13}CO spectrum averaged over the elliptical aperture.

The column density for ^{12}CO J=3-2 is estimated assuming LTE and optically thin emission using the equation

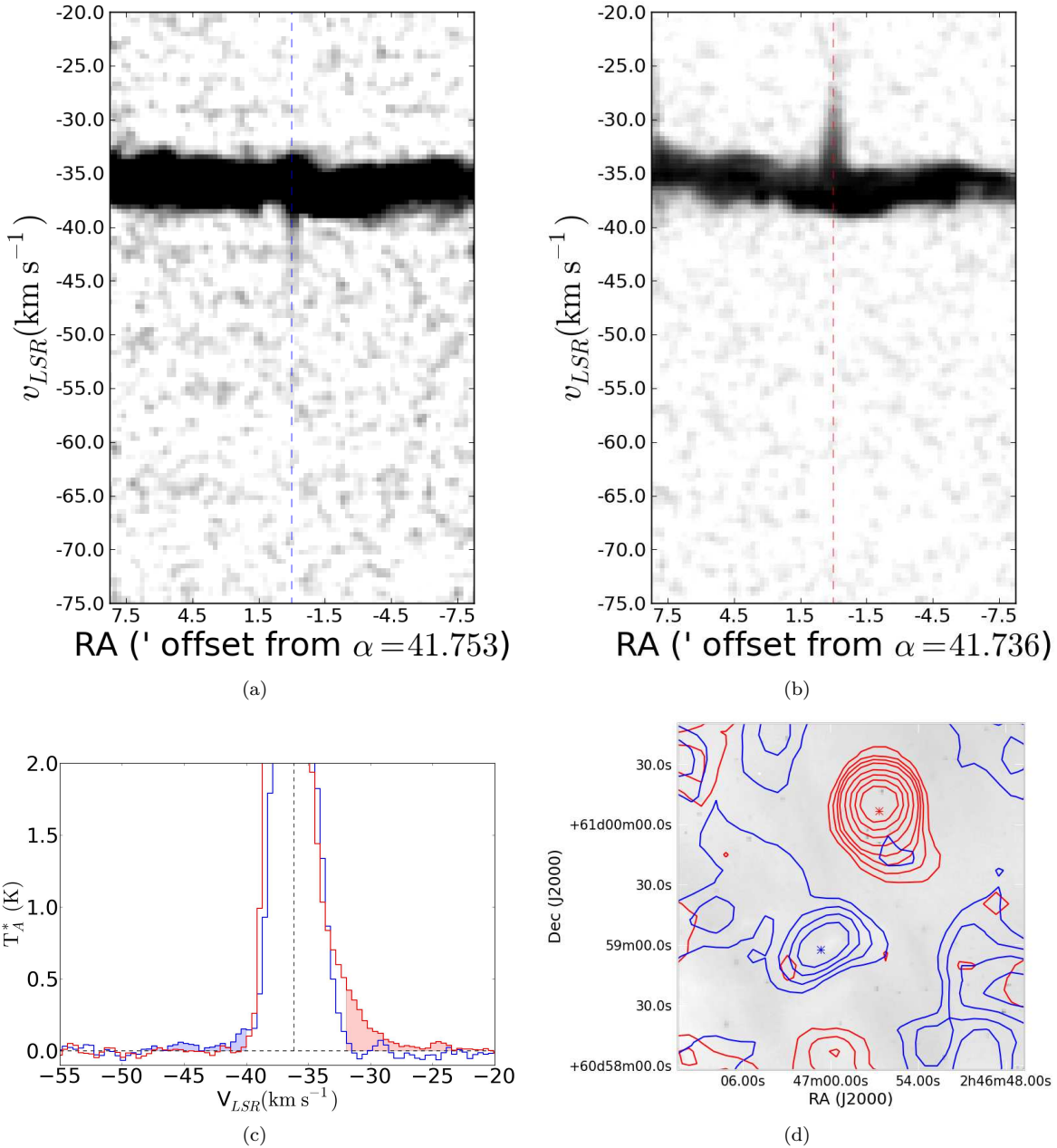


Figure 3. *Top:* Declination-velocity diagrams of Outflow 2, selected as an example because of its prominent redshifted flow and much weaker blueshifted counterpart. Left is the blue lobe, right is the red lobe. In this case, the redshifted lobe is much brighter and more obvious than the blue. The diagrams are displayed with an arcsinh stretch from 0 to 1 K (left) and 0 to 3 K (right). *Bottom Left:* Spectrum of both outflows superposed. The integration limits are indicated by shading. *Bottom Right:* Contours of the red and blue outflows superposed on the Spitzer 8 μ m image (which, in this region, is nearly flat). The contours are generated from a total intensity image integrated over the indicated outflow velocities. They are displayed at levels of 0.5, 1, 1.5, 2, 3, 4, 5, 6 K km s $^{-1}$ ($\sigma \approx 0.25$ K km s $^{-1}$).

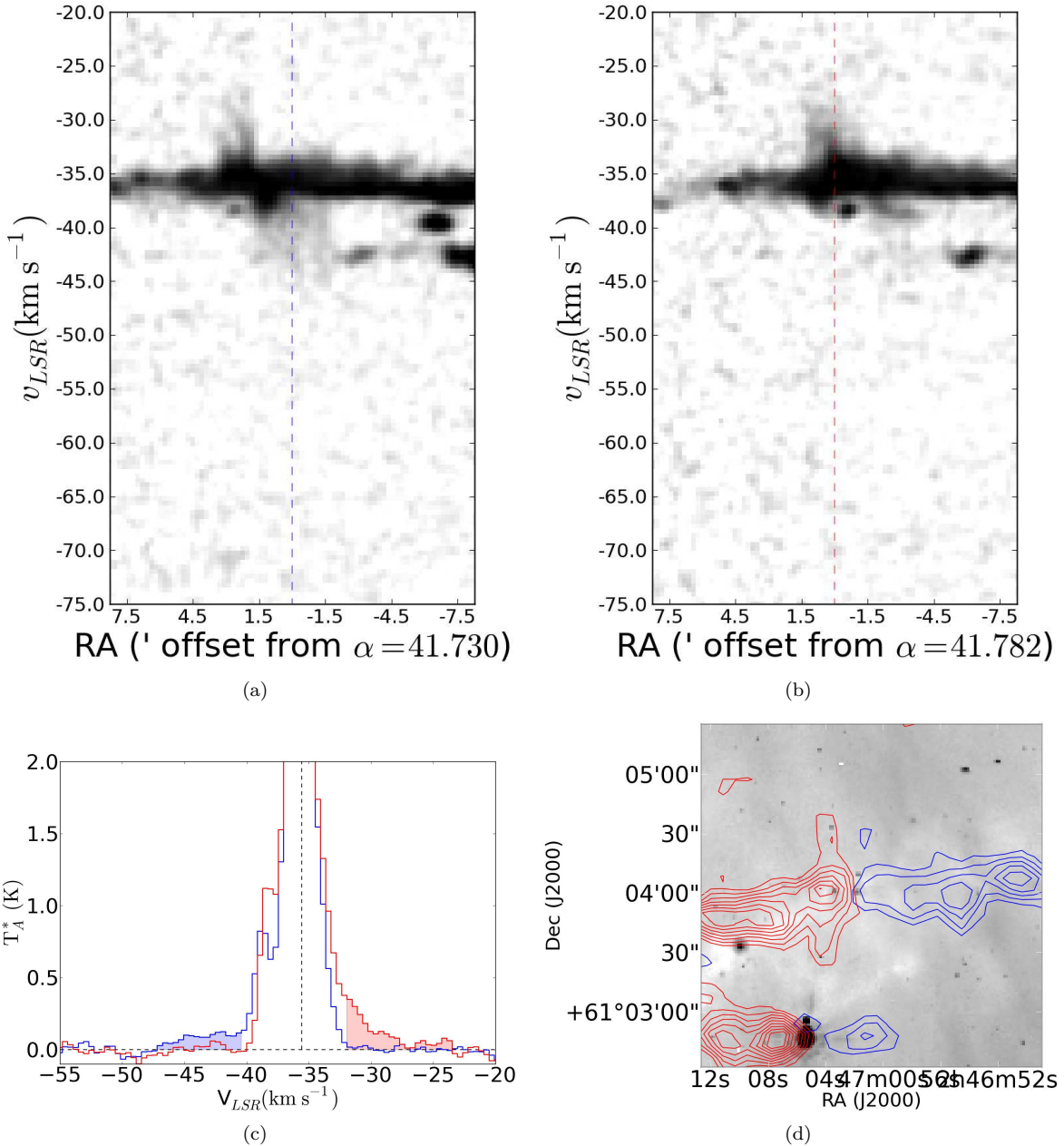


Figure 4. Top: RA-velocity diagrams of Outflow 1, which is the only outflow with very clearly resolved red and blue emission lobes. Left is the blue lobe, right is the red lobe. The diagrams are displayed with an arcsinh stretch from 0 to 3 K. Both display extended high velocity emission in the RA direction. Bottom Left: Spectrum of both outflows superposed. The integration limits are indicated by shading. Bottom Right: Contours of the red and blue outflows superposed on the Spitzer 8 μ m image. The contours are generated from a total intensity image integrated over the indicated outflow velocities. They are displayed at levels of 0.5, 1, 1.5, 2, 3, 4, 5, 6 K km s $^{-1}$ ($\sigma \approx 0.25$ K km s $^{-1}$).

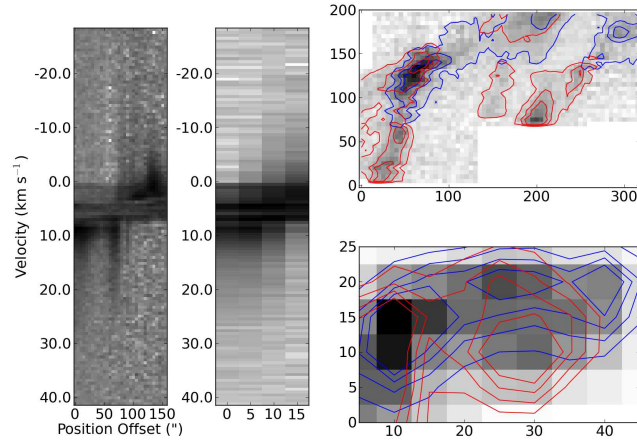


Figure 5. Comparison of L1448 seen at a distance of 250 pc (left) versus 2 kpc (middle) with sensitivity 0.5 K and 0.05K per 0.5 km s^{-1} channel respectively. *Far Left:* Position-velocity diagram (log scale) of the outflow L1448 IRS2 at its native resolution and velocity. L1448 IRS2 is the rightmost outflow in the contour plots. The PV diagram is rotated 45° from RA/Dec axes to go along the outflow axis. *Middle Left:* Position-velocity diagram (log scale) of the same outflow smoothed and rebinned to be eight times more distant. *Top Right:* The integrated map is displayed at its native resolution (linear scale). The red contours are of the same data integrated from 6.5 to 16 km s^{-1} and the blue from -6 to 0 km s^{-1} . Contours are at 1.3, and 5 K $km\ s^{-1}$ ($\sim 6, 18, 30\sigma$). Axes are offsets in arcseconds. *Bottom Right:* The same map as it would be observed at eight times greater distance. Axes are offsets in arcseconds assuming the greater distance. Contours are integrated over the same velocity range as above, but are displayed at levels 0.25, 0.50, 0.75, 1.00 K $km\ s^{-1}$ ($\sim 12, 24, 48, 60\sigma$). The entire region is detected at high significance, but dominated by confusion. It is still evident that the red and blue lobes are distinct, but they are each unresolved.

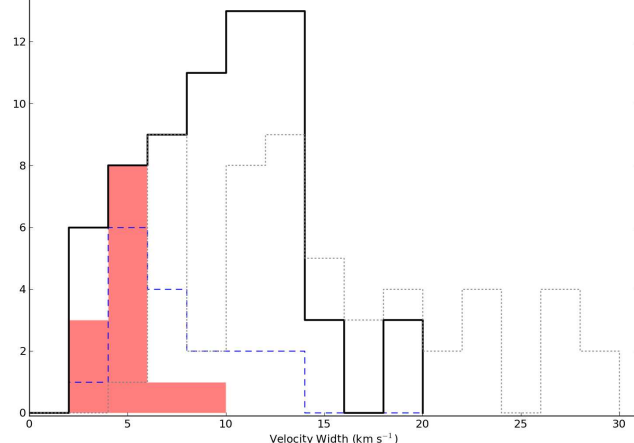


Figure 6. Histogram of the outflow widths. *Black lines:* histogram of the measured outflow widths (half-width zero-intensity, measured from the fitted central velocity of the cloud to the highest velocity with non-zero emission). *Blue dashed lines:* outflow HWZI for the outer arm (non-W5) sample. *Solid red shaded:* The measured widths (FWHM) of the sub-regions as tabulated in Table 1. *Gray dotted:* Outflow v_{max} (Half-width-1- σ) values for Perseus from Curtis et al. (2010).

$N_{\text{H}_2} = 5.3 \times 10^{18} \frac{1}{\eta_{mb}} \int T_A^*(v) dv$ for $T_{ex} = 20\text{K}$. Details on the derivation of this equation are given in the Appendix.

The scalar momentum and energy were computed using the equations

$$p = M \sum \frac{T_A^*(v)(v - v_c)\Delta v}{\sum T_A^*(v)\Delta v} \quad (1)$$

$$E = \frac{M}{2} \sum \frac{T_A^*(v)(v - v_c)^2 \Delta v}{\sum T_A^*(v)\Delta v} \quad (2)$$

where v_c is the ^{13}CO centroid velocity.

We compute the momentum flux using the simplest practical method. We estimate an outflow lifetime by taking half the distance between the red and blue outflow centroids divided by the maximum measured velocity difference ($\Delta v_{max} = v_{max,red} - v_{max,blue}$), $\tau_{flow} = r_{flow}/\Delta v_{max}$. This method assumes that the outflow inclination is 45° ; if it is more parallel to the plane of the sky, we overestimate the age, and vice-versa. The momentum flux is then $\dot{P} = p/\tau$. Similarly, we compute a mass loss rate by dividing the total outflow mass by the dynamical age, which yields what is most likely a lower limit on the mass loss rate (if the lifetime is underestimated, the mass loss rate is overestimated, but the outflow mass is always a lower limit because of optical depth and confusion effects).

The dynamical ages are highly suspect since the red and blue lobes are often unresolved or barely resolved, and diffuse emission averaged with the lobe emission can shift the centroid position. Additionally, it is not clear what portion of the outflow we centroid on when using ellipses that include all detected outflow emission - the bow shock or the jet could both potentially dominate the outflow emission. Curtis et al. (2010) include extensive discussion of the many ways in which the dynamical age can be mistaken. Nonetheless, the derived momentum fluxes (Figure 8) are within a reasonable range considering that W5 is a more active region of star formation than Perseus.

Because the emission was assumed to be optically thin, the mass, column, energy, and momentum measurements we present are strictly lower limits. It is likely that most of the emission from these outflows is blended with the host cloud emission. While some authors have computed correction factors to ^{12}CO 1-0 optical depths (e.g. Cabrit & Bertout 1990), our data are not of high enough spatial resolution to warrant these corrections, and the corrections are different for the 3-2 transition (1.8 to 14.3, Curtis et al. 2010). Additionally, CO 3-2 may require a substantial correction for being sub-thermally excited because of its higher critical density (the CO 3-2 critical density is 27 times higher than CO 1-0, see Appendix A for modeling of this effect).

The total measured outflow mass in W5 outflows is $M_{tot} = 1.5M_\odot$, substantially lower, even with optical depth correction $\approx 10\times$, than the $163 M_\odot$ reported in Perseus (Arce et al. 2010). The total outflow momentum is $p_{tot} = 10.9 M_\odot \text{ km s}^{-1}$. Assuming a turbulent line width $\Delta v \sim 3 \text{ km s}^{-1}$ (approximately the smallest line-width observed), the total turbulent momentum in the ambient cloud gas is $p = M_{tot}\Delta v = 7.8 \times 10^4 M_\odot \text{ km s}^{-1}$, which is $\sim 10^4$ times the measured current outflow momentum - the outflows detected in our survey cannot be the sole source of the observed turbulent line widths. In Table 1, we present the turbulent momentum for each sub-region computed by multiplying the

measured velocity with by the integrated ^{13}CO mass. Even if our outflow measurements are an order of magnitude low because of optical depth, cloud blending, sub-thermal excitation, and other missing-mass considerations, outflows contribute negligibly to the total outflow momentum in W5. This result is unsurprising, as there are many other likely sources of energy in the region such as stellar wind bubbles and shock fronts between the ionized and molecular gas.

Figure 7 displays the distribution of measured properties and compares them to those derived in the COMPLETE (Arce et al. 2010) and Curtis et al. (2010) HARP-B CO 3-2 surveys of Perseus. Our derived masses are substantially lower than those in Arce et al. (2010), but our momenta are similar to the CPOC sample and our energies are higher, indicating that we are highly biased towards detecting mass at high velocities, and in fact *more* biased towards high velocities than the CO 1-0 used in Arce et al. (2010). The discrepancy between our values and those of Arce et al. (2010) and Curtis et al. (2010) can be partly accounted for by the optical depth correction applied in those works: ^{13}CO was used to correct for opacity at low velocities, where most of the outflow mass is expected. In Curtis et al. (2010), this correction factor ranged from 1.8 to 14.3; Arce et al. (2010) did not directly quantify the optical depth correction they used but it is typically around 7 (Cabrit & Bertout 1990).

The momentum flux and mass loss rate are compared to the values derived in Perseus by Hatchell et al. (2007) and Curtis et al. (2010) in Figures 8 and 9. Both of our values are computed using the dynamical timescale τ_d measured from outflow lobe separation, while the Hatchell et al. (2007) values are derived using a more complicated direct momentum-flux measurement.

3.2 Large-scale cloud structure: Thin sheet

The W5 complex extends $\sim 1.6^\circ \times 0.7^\circ$ within 20° of parallel with the galactic plane. At the assumed distance of 2 kpc, it has a projected length of ~ 60 pc (Figure 2). In the $8 \mu\text{m}$ band (Figure 1), the region appears to consist of two blown-out bubbles with $\sim 10 - 15$ pc radii centered on $\ell = 138.1, b = 1.4$ and $\ell = 137.5, b = 0.9$. While the bubbles are filled in with low-level far-infrared emission, there is no CO detected down to a $3-\sigma$ limit of 3.0 K km s^{-1} (^{12}CO 1-0), 2.4 K km s^{-1} (^{12}CO 3-2, excepting a few isolated clumps), and 1.5 K km s^{-1} (^{13}CO 1-0). The strictest column limit comes from the ^{12}CO 3-2 observations (assuming LTE, $\tau \ll 1$, and $T_{ex} = 20\text{K}$), with a $3 - \sigma$ column limit $N_{\text{H}_2} < 7.8 \times 10^{18}$ within an $18''$ beam, or $A_V \lesssim 0.1$ magnitudes (using the Bohlin et al. 1978, A_V conversion). Individual ‘wisps’ and ‘clumps’ of CO can sometimes be seen, particularly towards the cloud edges, but in general the bubbles are absent of CO gas.

Given such low column limits, W5 must be seen nearly face-on in a thin sheet-like geometry; there can be no molecular gas behind the bubbles either. Alternately, along the line-of-sight, the columns of molecular gas are too low for CO to self-shield, and it is therefore destroyed by the UV radiation of W5’s O-stars. In either case, there is a significant excess of molecular gas in the plane of the sky compared to the line of sight, which makes W5 an excellent location to perform unobscured observations of the star formation process.

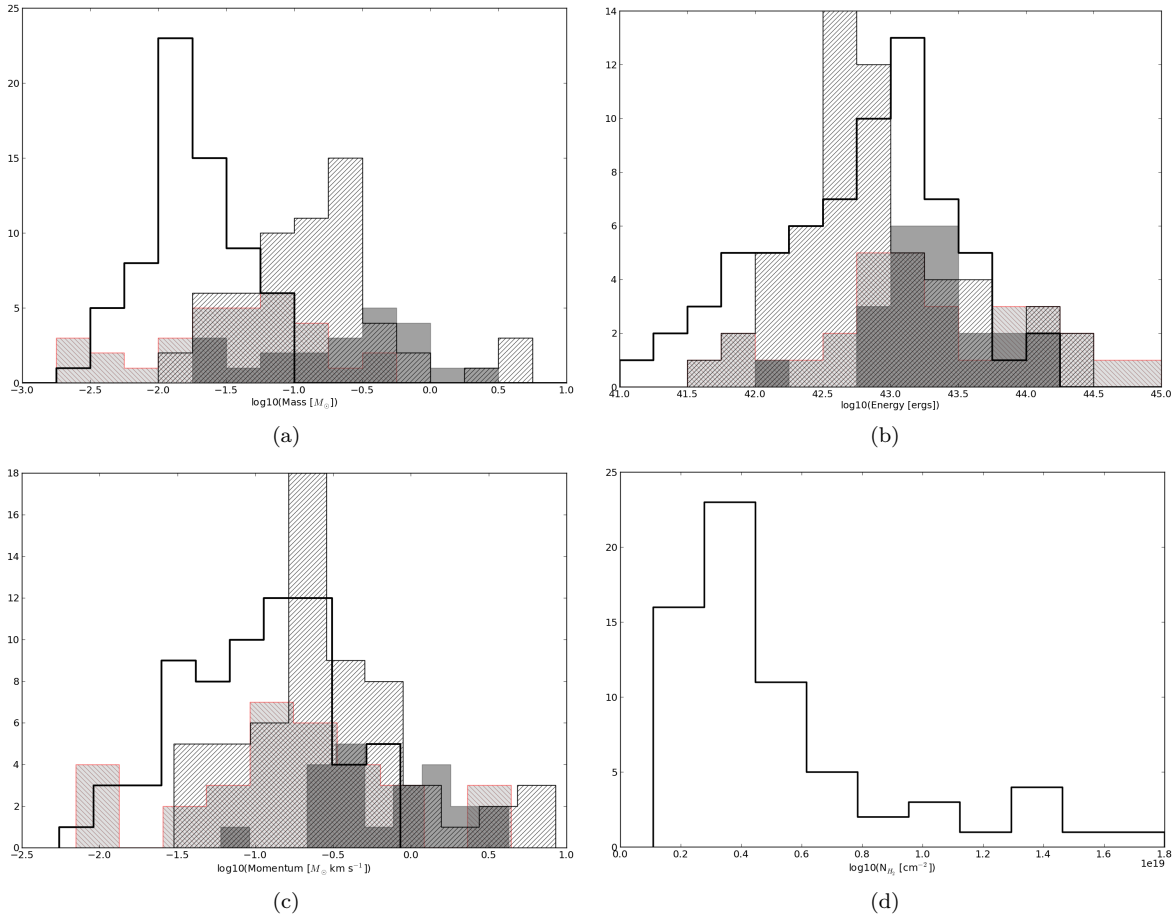


Figure 7. Histograms of outflow physical properties. The solid unfilled lines are the W5 outflows (this paper), the forward-slash hashed lines show Arce et al. (2010) CPOCs (outflow candidates), the dark gray shaded region shows Arce et al. (2010) values for known outflows in Perseus, and the light gray, backslash-hashed regions show Curtis et al. (2010) CO 3-2 outflow properties. The outflow masses measured in Perseus are systematically higher because both surveys corrected for line optical depth using ^{13}CO . It is likely that CO 3-2 is sub-thermally excited in outflows, and CO outflows may be destroyed by UV radiation in the W5 complex while they easily survive in the lower-mass Perseus region.

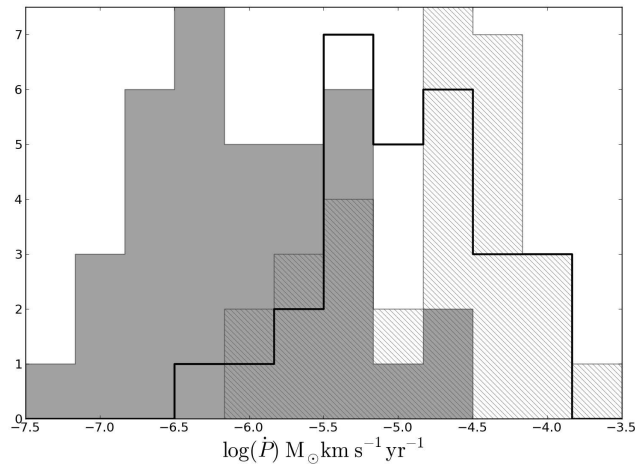


Figure 8. Histogram of the measured outflow momentum fluxes. The black thick line shows our data, the grey shaded region shows the Hatchell et al. (2007) data, and the hatched region shows Curtis et al. (2010) values. Our measurements peak squarely between the two Perseus JCMT CO 3-2 works, although the Curtis et al. (2010) results include an opacity correction that our data do not, suggesting that our results are likely consistent with Curtis et al. (2010) but inconsistent with the Hatchell et al. (2007) direct measurement method.

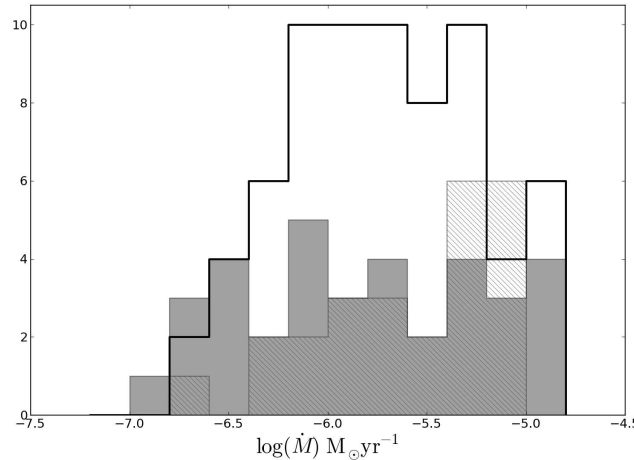


Figure 9. Histogram of the measured mass loss rate. The black thick line shows our data, while the grey shaded region shows the Hatchell et al. (2007) data, which is simply computed by $\dot{M} = \dot{P} \times 10/5 \text{ km s}^{-1}$, where the factor of 10 is a correction for opacity. Our mass loss rates are very comparable to those of Hatchell et al. (2007), but different methods were used so the comparison may not be physically meaningful. Curtis et al. (2010) (hatched) used a dynamical time method similar to our own and also derived similar mass loss rates, although their mass measurements have been opacity-corrected using the ^{13}CO 3-2 line.

There is also substantial morphological evidence supporting the face-on hypothesis. In the AFGL 4029 region (Section 4.2.2) and all along the south of W5, there are ridges with many individual cometary ‘heads’ pointing towards the O-stars that are unconfused along the line of sight. This sort of separation would not be expected if we were looking through the clouds towards the O-stars. W5W, however, presents a counterexample in which there are two clouds along the line of sight that may well be masking a more complex geometry.

3.3 Sub-regions

Individual regions were selected from the mosaic for comparison. All regions with multiple outflows and indicators of star formation activity were named and include as regions for analysis. Additionally, three “inactive” regions were selected based on the presence of ^{13}CO emission but the lack of outflows in the ^{12}CO 3-2 data. Finally, two regions devoid of CO emission were selected as a baseline comparison. The regions are identified on the integrated ^{13}CO image in Figure 10.

Average spectra were taken of each “region” within the indicated box. Gaussians were fit to the spectrum to determine line-widths and centers (Figure 11, Table 1). Gaussian fits were necessary because in many locations there are at least two velocity components, so the second moment (the “intensity-weighted dispersion”) is a poor estimator of line width. Widths ranged from $v_{FWHM} = 2.3$ to 6.2 km s^{-1} (Figure 6).

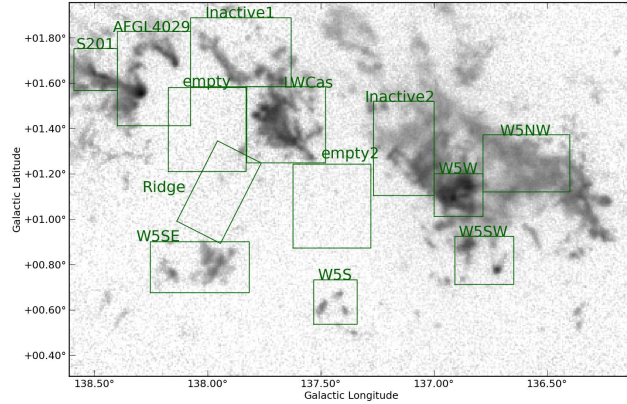


Figure 10. Individual region masks overlaid on the FCRAO ^{12}CO integrated image. The named regions, S201, AFGL4029, LWCas, W5NW, W5W, W5SE, W5S, and W5SW, were all selected based on the presence of outflows within the box. The inactive regions were selected from regions with substantial CO emission but without outflows. The ‘empty’ regions have essentially no CO emission within them and are used to place limits on the molecular gas within the east and west ‘bubbles’.

Table 1. Gaussian fit parameters of sub-regions

Region	Velocity 1 (km s ⁻¹)	Width 1 (σ , km s ⁻¹)	Amplitude 1 (K)	Velocity 2 (km s ⁻¹)	Width 2 (σ , km s ⁻¹)	Amplitude 2 (K)	¹³ COmass M_{\odot}	¹³ COMomentum M_{\odot} km s ⁻¹
S201	-38.04	1.89	2.35	-	-	-		
AFGL4029	-38.91	2.02	1.48	-	-	-		
LWCas	-38.83	2.09	2.33	-	-	-		
W5W	-41.37	2.33	3.07	-36.16	2.30	1.90		
W5NW	-36.37	2.31	1.6	-	-	-		
W5SW	-42.78	2.49	0.6	-36.34	2.51	0.22		
W5S	-40.15	1.76	0.34	-35.76	1.36	0.40		
Inactive1	-42.91	1.6	0.75	-39.38	2.53	0.42		
Inactive2	-38.94	2.24	1.2	-	-	-		
empty	-37.81	3.14	0.04	-	-	-		

¹³CO fits

S201	-37.97	1.55	0.56	-	-	-	1400	5200
AFGL4029	-38.66	1.41	0.35	-	-	-	2700	8900
LWCas	-38.75	1.62	0.51	-	-	-	3900	15000
W5W	-41.23	1.67	1.09	-36.51	2.14	0.47	4600	42000
W5NW	-36.1	2.07	0.7	-	-	-	5500	27000
W5SW	-42.6	2.29	0.1	-36.15	2.56	0.05	820	9300
W5S	-39.9	1.47	0.07	-35.48	1.33	0.08	330	2200
Inactive1	-42.58	1.51	0.1	-38.97	1.70	0.07	1400	11000
Inactive2	-38.82	1.92	0.37	-	-	-	3200	14000
empty	-38.44	2.87	0.02	-	-	-	390	2600

4 DISCUSSION

4.1 Comparison to other outflows

The outflow properties we derive are similar to those in the B0-star forming clump IRAS 05358+3543 ($M \approx 600M_{\odot}$ Ginsburg et al. 2009), in which CO 3-2 and 2-1 were used to derive outflow masses in the range 0.01-0.09 M_{\odot} . However, some significantly larger outflows, up to 1.6 pc in one direction were detected, while the largest resolved outflow in our survey was only 0.8 pc (one direction). With 54 detected outflows across a star-forming region that includes many young B-stars, the lack of long outflows is somewhat surprising and suggests that outflows in W5 are truncated. One likely explanation is that the outflows burst out of the cloud and the CO molecules are dissociated by ionizing radiation from the HII region. This explanation is adequate to describe truncated outflows coming from cometary clouds and regions with illuminated edges. It can also be tested with a search for optically excited outflow tracers (Herbig-Haro objects and Molecular Hydrogen Objects) near clusters of CO outflows.

We noted in Section 3.1.1 that the average mass measured in our survey is lower than the Curtis et al. (2010) HARP CO 3-2 survey and much lower than the Arce et al. (2010) FCRAO COMPLETE CO 1-0 survey of Perseus. However, we measure comparable momenta and energy. From Figure 7, it is evident that there is also a discrepancy between the Curtis et al. (2010) and Arce et al. (2010) measurements. We suggest that this is likely because the excitation temperatures for the CO 3-2 transition is lower than CO 1-0 different. The discrepancy between our mass measurements and the Perseus mass measurements can be accounted for by opacity; applying a 7× correction factor (increase) to our data brings our distribution into agreement with Curtis et al. (2010).

4.2 Star Formation Activity

CO outflows are an excellent tracer of ongoing embedded star formation (e.g. Shu et al. 1987). We use the locations of newly discovered outflows to qualitatively describe the star formation activity within the W5 complex and evaluate the hypothesis that star formation has been triggered on small or intermediate scales.

Class 0/I objects are nearly always associated with outflows in nearby star-forming regions (e.g. Curtis et al. 2010; Hatchell et al. 2007). However, Koenig et al. (2008) detected ~ 170 Class I sources using Spitzer photometry. Since our detection threshold for outflow appears to be similar to that in Perseus (Section 3.1.1), the lower number of outflow detections is surprising, especially considering that some of the detected outflows are outside the Spitzer-MIPS field (MIPS detections are required for Class I objects, and flows 1-4 are outside that range) or are in the outer arm (flows 39-54). Additionally, we should detect outflows from Class 0 objects that would not be identified by Spitzer colors.

There are a number of explanations for the number discrepancy. The Class I objects detected within the HII region “bubble” most likely have outflows in which the CO is dissociated similar to jet systems in Orion (e.g. HH46/47, a pc-scale flow in which CO is only visible very near the protostar Chernin & Masson 1991; Stanke et al. 1999). This

hypothesis can be tested by searching for optical and infrared jets associated with these objects, which presumably have lower mass envelopes and therefore less extinction than typical Class I objects. Additionally, there are many outflow systems that are likely to be associated with clusters of outflows rather than individual outflows similar to the confusion shown in Section 3.1.1; in many cases there are multiple Koenig et al. (2008) Class I sources within the contours of a single outflow system.

4.2.1 *Sh 2-201*

Sh 2-201 is an HII region and is part of the same molecular cloud as the bright-rimmed clouds in W5E, but it does not share a cometary shape with these clouds (figure 12). Instead, it is internally heated and has its own HII region (Felli et al. 1987). The AFGL 4029 cloud edge is at a projected distance of ~ 7 pc, and the closest illuminated point in the Spitzer 8 and 24 μm maps is at a projected distance of ~ 5 pc. The star forming process must therefore have begun before radiation driven shocks from the W5 O-stars could have impacted the cloud.

4.2.2 *AFGL 4029*

AFGL 4029 is a young cluster embedded in a cometary cloud (figure 13). There is one clear bipolar outflow and 6 single-lobed flows that cannot be unambiguously associated with an opposite direction counterpart. The cluster is mostly unresolved in the data presented here and is clearly the most active clump. It contains a cluster of at least 30 B-stars (Deharveng et al. 1997).

The northeast cometary cloud is strongly affected by the HII region. It has an outflow in the head of the cloud (Figure 14), and the cloud shows a velocity gradient with distance from the HII region. The polarity of the gradient suggests that the cometary cloud must be on the far side of the ionizing O-star along the line of sight assuming that the HII region pressure is responsible for accelerating the cloud edge.

4.2.3 *W5 Ridge*

The W5 complex consists of two HII region bubbles separated by a ridge of molecular gas (figure 15). This ridge contains the LW Cas optical nebula, a reflection nebula around the variable star LW Cas, on its east side and an X-shaped nebula on the west. The east portion of LW Cas Nebula is bright in both the continuum and CO J=3-2 but lacks outflows (see Figure 15). The east portion also has the highest average peak antenna temperature, suggesting that the gas temperature in this region is substantially higher than in the majority of the W5 complex (higher spatial densities could also increase the observed T_A , but the nearby heating sources make a higher temperature more plausible). It is possible that high gas temperatures are suppressing star formation in the cloud. Alternately, the radiation that is heating the gas may destroy any outflowing CO, which is more likely assuming the two Class I objects identified in this region by Koenig et al. (2008) are genuine YSOs.

The ridge is surprisingly faint in HI emission compared

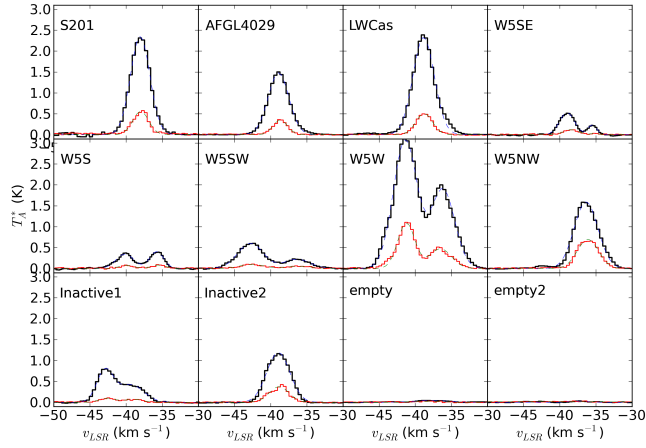


Figure 11. Spatially averaged spectra of the individual regions analyzed. ^{12}CO 3-2 is shown by thick black lines and ^{13}CO 1-0 is shown by thin red lines. Gaussian fits are overplotted in blue and green dashed lines, respectively. The fit properties are given in Table 1.

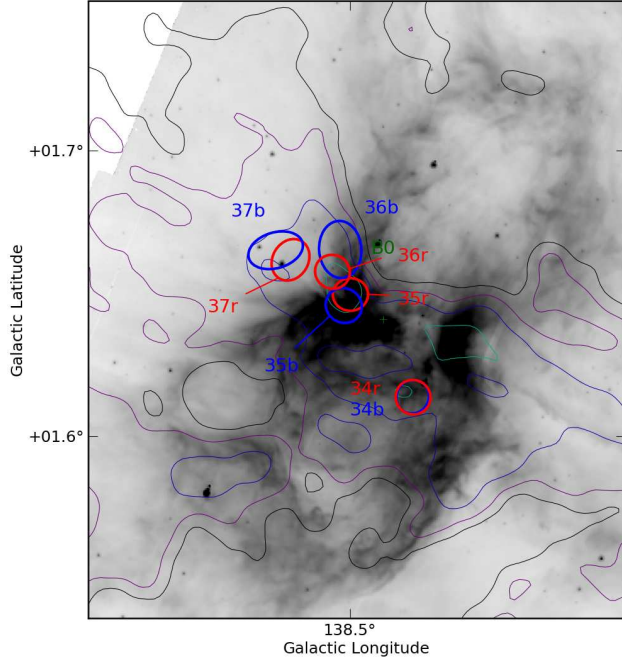


Figure 12. Small scale map of the Sh 2-201 region. The IRAC 8 μm image is displayed in inverted log scale from 800 to 8000 MJy sr^{-1} . Contours of the CO 3-2 cube integrated from -60 to -20 km s^{-1} are overlaid at logarithmically spaced levels from 3 to 100 K km s^{-1} ($3.0, 7.2, 17.3, 41.6, 100; \sigma \approx 0.7 \text{ K km s}^{-1}$).

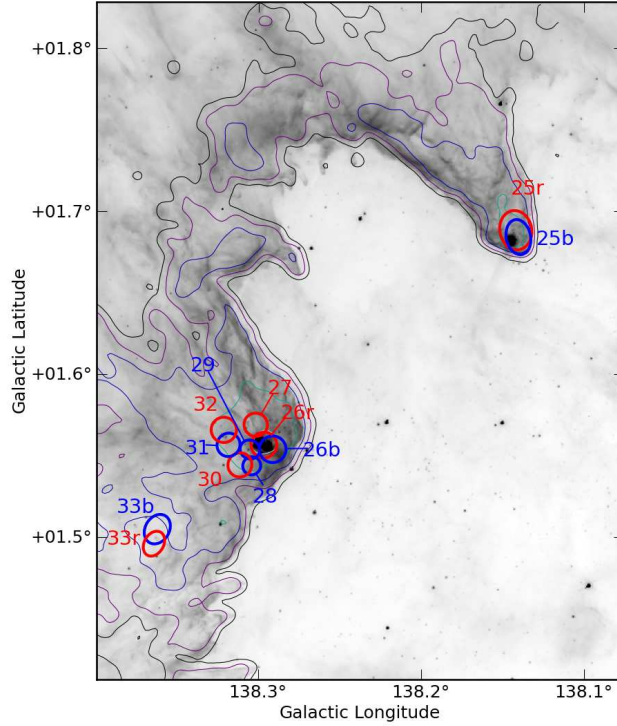


Figure 13. Small scale map of the AFGL 4029 region. The IRAC $8 \mu\text{m}$ image is displayed in inverted log scale from 800 to 8000 MJy sr^{-1} . Contours of the CO 3-2 cube integrated from -60 to -20 km s^{-1} are overlaid at logarithmically spaced levels from 3 to 100 K km s^{-1} ($3, 0.7, 2, 17, 3, 41, 6, 100$; $\sigma \approx 0.7 \text{ K km s}^{-1}$). Outflows 26-32 are ejected from a dense forming cluster. A diagram displaying the kinematics of the northern cometary cloud is shown in Figure 14.

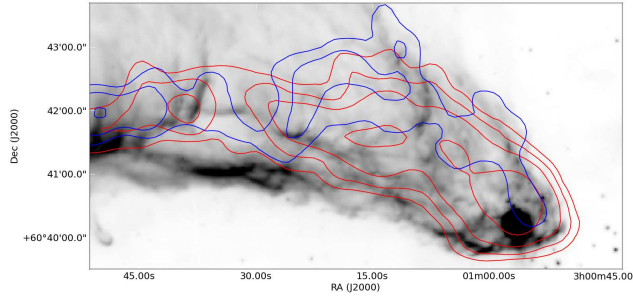


Figure 14. The northeast cometary cloud. Contours are shown at $0.5, 1, 2$, and 5 K km s^{-1} integrated over the ranges -44.0 to -41.9 km s^{-1} (blue) and -38.1 to -35.6 km s^{-1} (red). There is a velocity gradient across the tail, suggesting that the front edge is being pushed away along the line of sight.

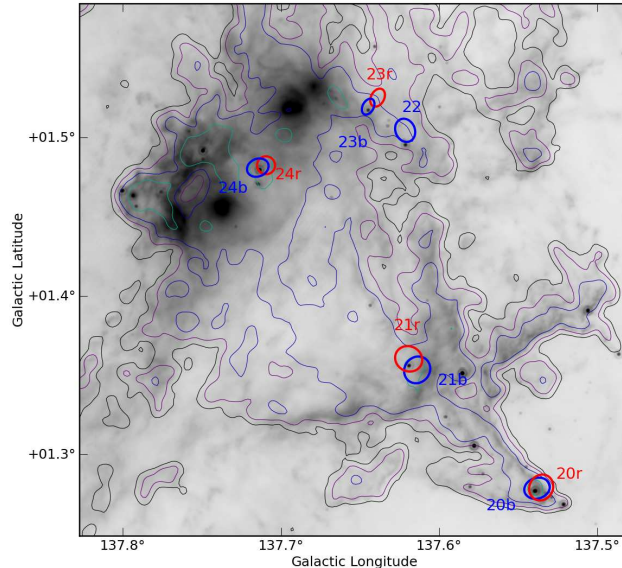


Figure 15. Small scale map of the LW Cas nebula. The feature containing outflows 20 and 21 is the X-shaped ridge referenced in Section 4.2.3. This sub-region is notable for having very few outflows associated with the most significant patches of CO emission. The $24\ \mu\text{m}$ source marked by an X at $J(2000) = 02:57:08.0233 +60:39:44.142$ is the B1V star BD+60 596. The gas around it is heated on the left side by the O7V star HD 18326 ($D_{proj} = 8.5$ pc), suggesting that this gas could be substantially warmer than the other molecular clouds in W5.

to the two HII regions (Figure 16) considering its $24\ \mu\text{m}$ surface brightness. The integrated HI intensity from -45 to $-35\ \text{km s}^{-1}$ is $\sim 800\ \text{K km s}^{-1}$, whereas in the HII region bubble it is around $1000\ \text{K km s}^{-1}$. The CO-bright regions show lower levels of emission similar to the ridge at $700\text{--}800\ \text{K km s}^{-1}$. However, the ridge contains no CO gas and very few young stars (Figure 7 in Koenig et al. 2008). It is possible that the ridge contains cool HI but has very low column-densities along the direction pointing towards the O-stars, in which case the self-shielding is too little to prevent CO dissociation. This ridge may therefore be an excellent location to explore the transition from molecular to atomic gas under the influence of ionizing radiation in conditions different from high-density photodissociation (photon-dominated) regions.

4.2.4 Southern Pillars

There are 3 cometary clouds that resemble the “elephant trunk” nebula in IC 1396 (Figure 17). Each of these pillars contains evidence of at least one outflow in the head of the cloud. These pillars are low-mass and isolated; there is no other outflow activity in southern W5. However, because of the bright illumination on their northern edges and robust star formation tracers, these objects present the strongest case for triggered star formation by the RDI mechanism in W5.

The kinematics of these cometary clouds suggest that they have been pushed in different directions by the HII region (Figure 17). The central cometary cloud has two tails. The southwest tail emission peaks around $-39.5\ \text{km s}^{-1}$ and the southeast tail peaks at $-41.5\ \text{km s}^{-1}$, while the head is peaked at an intermediate $-40.5\ \text{km s}^{-1}$. These velocity shifts suggest that the gas is being accelerated perpendicular to the head-tail axis and that the southeast tail is on the

back side of the cometary head, while the southwest tail is on the front side. Therefore the HII region is crushing this head-tail system.

The southeast (left) cometary cloud peaks at $-35.0\ \text{km s}^{-1}$. There are no clearly-separated CO tails as in the central cloud, but there is a velocity shift across the tail, in which the west (right) side is blueshifted compared to the east (left) side, which is the opposite sense from the central cometary cloud.

The southwest (right) cometary cloud peaks at $-40.3\ \text{km s}^{-1}$ and has weakly defined tails similar to the central cloud. Both of its tails are at approximately the same velocity ($-42.5\ \text{km s}^{-1}$).

The kinematics of these tails provide some hints of their 3D structure and location in the cloud. Future study to compare the many cometary flows in W5 to physical models and simulations is warranted. Since these flows are likely at different locations along the line of sight (as required for their different velocities), analysis of their ionized edges may allow for more precise determination of the full 3D structure of the clouds relative to their ionizing sources.

4.2.5 W5 Southeast

The region identified as W5SE has very little star formation activity despite having significant molecular gas ($M_{13\text{CO}} \sim 800M_{\odot}$). While there are two outflows and two Class I objects Koenig et al. (2008) in the southeast of the two clumps ($\ell = 138.15, b = 0.77$), the main clump ($\ell = 138.0, b = 0.8$) has no detected outflows. The CO emission is particularly clumpy in this region, with many independent, unresolved clumps both in position and velocity. In the 8 and 24 micron Spitzer images, it is clear that these clouds are illuminated from the northwest. This region represents a case in which the expanding HII region has impacted molecular gas but

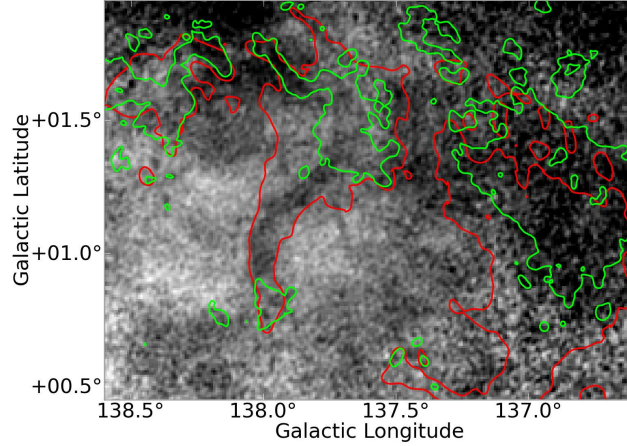


Figure 16. The DRAO 21 cm HI map integrated from -45 to -35 km s $^{-1}$ displayed in grayscale from 700 to 1200 K km s $^{-1}$ with IRAS $100 \mu\text{m}$ contours (red, 40 MJy sr^{-1}) and ^{12}CO 1-0 contours integrated over the same range (green, 4 K km s^{-1}) overlaid. The ridge of IRAS $100 \mu\text{m}$ emission at $\ell = 138.0$ coincides with a relative lack of HI emission.

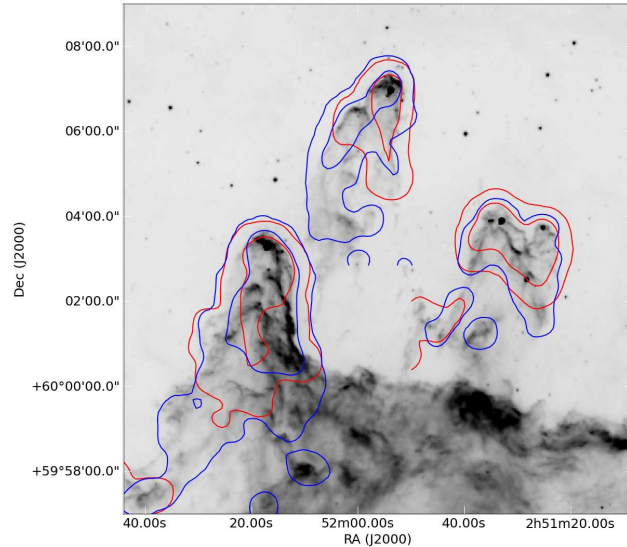


Figure 17. CO 3-2 contours overlaid on the Spitzer 8 μm image of the W5S cometary clouds described in Section 4.2.4. The contours are shown at different velocities for each cometary cloud at levels of $T_A^* = 0.25, 3 \text{ K}$ in order to illustrate the velocity gradients. Southeast: -34.2 km s^{-1} (red), -36.6 km s^{-1} (blue); Central: -39.2 km s^{-1} (red), -41.9 km s^{-1} (blue); Southwest: -40.6 km s^{-1} (red), -41.4 km s^{-1} (blue).

has not triggered additional star formation. The high clump-to-clump velocity dispersion observed in this region may be analogous to the W5S cometary clouds (Section 4.2.4) but without condensed clumps around which to form cometary clouds.

4.2.6 W5 Southwest

There is an isolated clump associated with outflows in the southwest part of W5 (figure 18) at $v_{LSR} \sim -45 \text{ km s}^{-1}$. While this clump is likely to be associated with the W5 region, it shows little evidence of interaction with the HII region. If it is eventually impacted by the expanding ionization front (i.e. if it is within the W5 complex), this clump will be an example of “revealed”, not triggered, star formation. The other source in W5SW is a cometary cloud with a blueshifted head and redshifted tail (Figure 19). The head contains a redshifted outflow; no blueshifted counterpart was detected.

4.2.7 W5 West / IC 1848

There is a bright infrared source seen in the center of W5W (IRAS 02459+6029; Figure 20), but the nearest CO outflow lobe is $\approx 1 \text{ pc}$ away. The nondetection may be due to confusion in this area - there are two layers of CO gas separated by $\sim 5 \text{ km s}^{-1}$, so low-velocity outflow detection is more difficult; the minimum detectable velocity in this region is $\sim 10 \text{ km s}^{-1}$. Unlike the rest of the W5 complex, this region appears to have multiple independent confusing components along the line of sight, and therefore the CO data provide much less useful physical information.

4.2.8 W5 NW

The northwest cluster (figure 22) containing outflows 1-8 is at a slightly different velocity ($\sim -35 \text{ km s}^{-1}$) than the majority of the W5 cloud complex ($\sim -38 \text{ km s}^{-1}$; Figure 21), but is shares contiguous emission with the neighboring W5W region. Its existence suggests that small- to intermediate-scale triggering is not responsible for the current generation of star formation throughout W5: this cluster shows much lower CO surface temperatures and weaker Spitzer $8 \mu\text{m}$ emission than the “bright-rimmed clouds” seen near the W5 O-stars and therefore has not been affected by their radiation. The presence of independent but co-eval star formation is, however, consistent with the large-scale “collect-and-collapse” triggering scenario.

4.2.9 Outflow systems in the Outer Arm and beyond

Just south of Sh 2-201, there is a bipolar outflow with a high velocity $v_{LSR}(^{12}\text{CO } 3-2) = -59.6 \text{ km s}^{-1}$. At its kinematic distance of 5.5 kpc , it is at a galactocentric radius of about 12.3 kpc .

Three high-velocity outflows are observed in the W5W region, around $\ell = 136.4, b = 1.0$, in outer-arm CO complexes noted by Digel et al. (1996). Outflows 41 - 44 are associated with a cloud at $v_{LSR} \sim -62 \text{ km s}^{-1}$ (known in the literature as LDN 1375), which corresponds to a kinematic distance $d = 5.5 \text{ kpc}$ and galactocentric distance $D_G = 13.0$

kpc. Outflow 40 is the furthest in our survey, at a kinematic distance $d = 7.5 \text{ kpc}$ ($v_{lsr} = -75.6 \text{ km s}^{-1}$) and galactocentric distance $D_G = 14.7 \text{ kpc}$.

There is a region in the southwest around $\ell = 136.8, b = 0.4$ at $v_{LSR} \sim -61 \text{ km s}^{-1}$ that likely contains at least one outflow, but it has two wide ($\sim 5 \text{ km s}^{-1}$) components that act to mask any outflows that may be present.

When corrected for distance, these outflows are among the most massive in our survey, though in table 2 their properties are shown assuming a distance of 2 kpc for consistency. These outflows are very unlikely to be associated with the W5 complex based on its velocity, so they are excluded from the combined analysis.

5 CONCLUSIONS

We have identified 40 molecular outflows in the W5 star forming region and an additional 15 outflows spatially coincident but located in the outer arm of the Galaxy.

- The majority of the CO clouds in the W5 complex are forming stars. Star formation is not limited to cloud edges around the HII region. Because star formation activity is observed outside of the region of influence of the W5 O-stars, it is apparent that the radiatively-driven implosion mechanism does not explain all of the star formation in W5.
- The W5 complex is seen nearly face-on as evidenced by a strict upper limit on the CO column through the center of the HII-region bubbles. It is therefore an excellent region to study massive star feedback and revealed and triggered star formation.
- Outflows contribute negligibly to the turbulent energy of molecular clouds in the W5 complex. This result is unsurprising near an HII region, but supports the idea that massive star forming regions are qualitatively different from low-mass star-forming regions in which the observed turbulence can be explained by outflow feedback.
- Despite detecting a significant number of powerful outflows, the total outflowing mass detected in this survey ($\sim 1.5 M_\odot$) was small compared to Perseus, a low to intermediate mass star forming region.
- We suggest that the low mass measured is partly because the CO 3-2 line is sub-thermally excited in outflows. Therefore, while CO 3-2 is an excellent tracer of outflows for detection, it does not serve as a ‘calorimeter’ in the same capacity as CO 1-0.
- Outflows have been detected in the Outer Arm at galactocentric distances $\gtrsim 12 \text{ kpc}$. These represent some of the highest galactocentric distance star forming regions discovered to date.
- Velocity gradients across the tails of many cometary clouds have been observed. The data presented contain tens of cometary clouds with precise kinematic information about their molecular gas.

6 ACKNOWLEDGEMENTS

This work has made use of the APLpy plotting package (<http://aplpy.sourceforge.net>), the pyregion package (<http://leejjoon.github.com/pyregion/>), the agpy code package (<http://code.google.com/p/agpy/>)

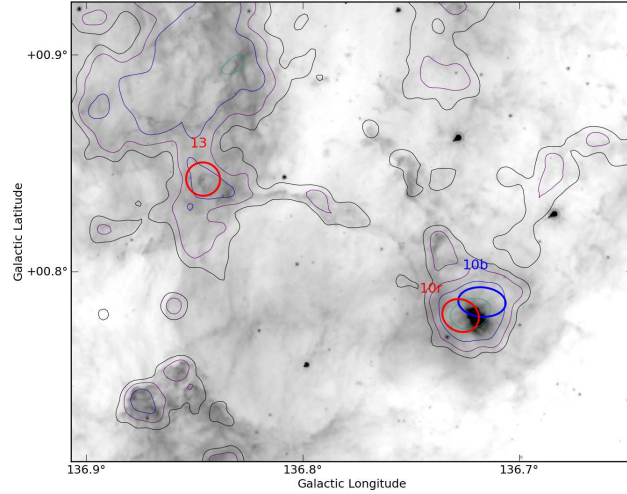


Figure 18. Small scale map of the W5 SW region. Outflow 13 is at the head of a cometary cloud (Figure 19) and therefore has clearly been affected by the expanding HII region, but the region including bipolar Outflow 10 shows no evidence of interaction with the HII region.

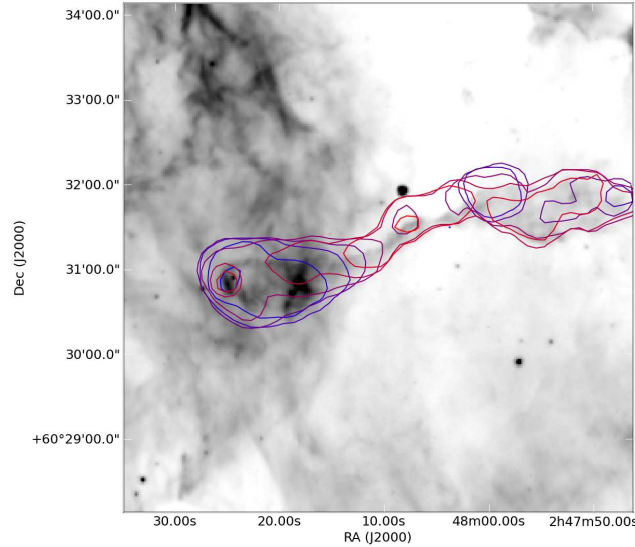


Figure 19. The cometary cloud in the W5 Southwest region (Outflow 13). Contours are shown at 1 K km s⁻¹ for 1 km s⁻¹ wide channels from -37.2 km s⁻¹ (blue) to -30.5 km s⁻¹ (red). The head is clearly blueshifted relative to the tail and contains a spatially unresolved redshifted outflow.

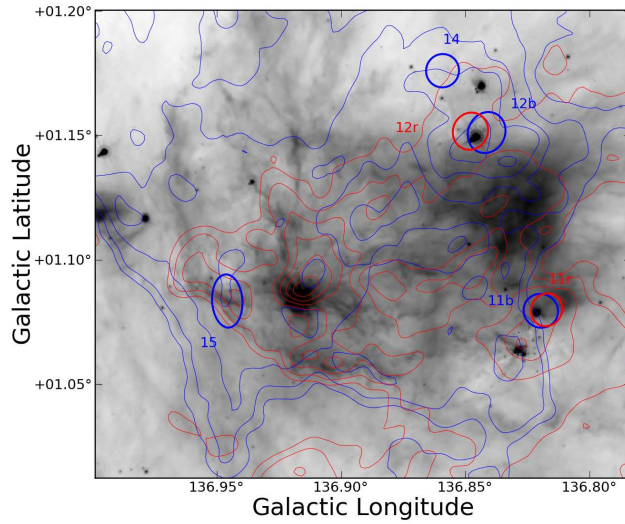


Figure 20. Small scale map of the W5 W region. The IRAC $8 \mu\text{m}$ image is displayed in inverted log scale from 800 to 8000 MJy sr^{-1} . Contours of the CO 3-2 cube integrated from -50 to -38 km s^{-1} (blue) and -38 to -26 km s^{-1} (red) are overlaid at levels $5, 10, 20, 30, 40, 50, 60 \text{ K km s}^{-1}$. $\sigma \approx 0.5 \text{ K km s}^{-1}$. The lack of outflow detections is partly explained by the two spatially overlapping clouds that are adjacent in velocity.

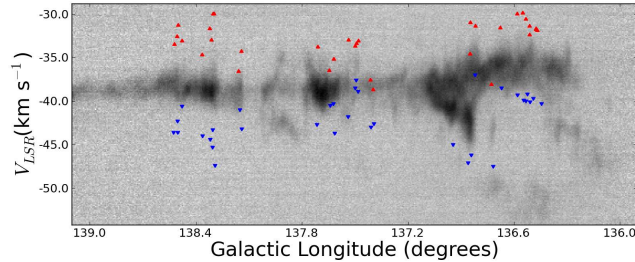


Figure 21. Integrated longitude-velocity diagram of the W5 complex from $b = 0.25$ to $b = 2.15$ in ^{12}CO 1-0 from the FCRAO OGS. The W5NW region is seen at a distinct average velocity around $\ell = 136.5$, $v_{LSR} = -34 \text{ km s}^{-1}$. The red and blue triangles mark the longitude-velocity locations of the detected outflows. In all cases, they mark the low-velocity start of the outflow.

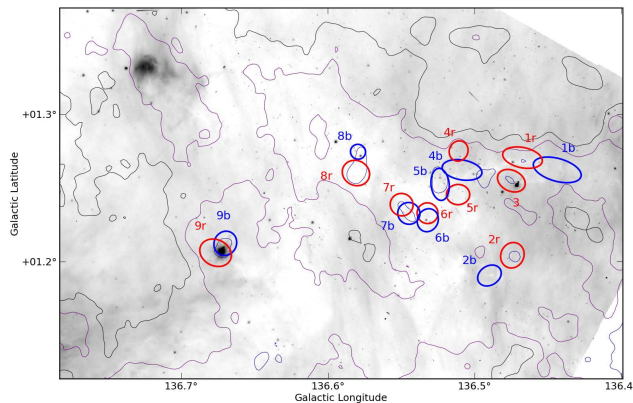


Figure 22. Small scale map of the W5 NW region. Despite its distance from the O-stars previously suspected to be responsible for triggering star formation around the edges of the W5 bubble, $D_{proj} \approx 20 \text{ pc}$, this cluster is the most active site of star formation in the complex as measured by outflow activity.

, IPAC's Montage (<http://montage.ipac.caltech.edu/>), the DS9 visualization tool (<http://hea-www.harvard.edu/RD/ds9/>), and the STARLINK package (<http://starlink.jach.hawaii.edu/>). IRAS data was acquired through IRSAT at IPAC (<http://irsa.ipac.caltech.edu/>). DRAO 21 cm data was acquired from the Canadian Astronomical Data Center (<http://cadcwww.hia.nrc.ca/cgps/>). The authors are supported by the National Science Foundation through NSF grant AST-0708403.

REFERENCES

- Adams, F. C. & Fatuzzo, M. 1996, *ApJ*, 464, 256
- Arce, H. G., Borkin, M. A., Goodman, A. A., Pineda, J. E., & Halle, M. W. 2010, *The Astrophysical Journal*, 715, 1170
- Bachiller, R. 1996, *ARA&A*, 34, 111
- Bertoldi, F. & McKee, C. F. 1990, *ApJ*, 354, 529
- Bohlin, R. C., Savage, B. D., & Drake, J. F. 1978, *ApJ*, 224, 132
- Bourke, T. L. et al. 1997, *ApJ*, 476, 781
- Bretherton, D. E., Moore, T. J. T., & Ridge, N. A. 2002, in Hot Star Workshop III: The Earliest Phases of Massive Star Birth, Vol. 267, 347
- Cabrit, S. & Bertout, C. 1990, *ApJ*, 348, 530
- Chernin, L. M. & Masson, C. R. 1991, *ApJ*, 382, L93
- Curtis, E. I., Richer, J. S., Swift, J. J., & Williams, J. P. 2010, *MNRAS*, 1304
- Deharveng, L., Zavagno, A., Cruz-Gonzalez, I., Salas, L., Caplan, J., & Carrasco, L. 1997, *A&A*, 317, 459
- Digel, S. W., Lyder, D. A., Philbrick, A. J., Puche, D., & Thaddeus, P. 1996, *ApJ*, 458, 561
- Elmegreen, B. G. 1998, in Astronomical Society of the Pacific Conference Series, Vol. 148, Origins, ed. C. E. Woodward, J. M. Shull, & H. A. Thronson Jr., 150–+
- Elmegreen, B. G. & Lada, C. J. 1977, *ApJ*, 214, 725
- Enoch, M. L. et al. 2006, *ApJ*, 638, 293
- Felli, M., Hjellming, R. M., & Cesaroni, R. 1987, *A&A*, 182, 313
- Garden, R. P., Hayashi, M., Hasegawa, T., Gatley, I., & Kaifu, N. 1991, *ApJ*, 374, 540
- Ginsburg, A. G., Bally, J., Yan, C., & Williams, J. P. 2009, *ApJ*, 707, 310
- Goldsmith, P. F. 1972, *ApJ*, 176, 597
- Hachisuka, K. et al. 2006, *ApJ*, 645, 337
- Hatchell, J. & Dunham, M. M. 2009, 0904.1163
- Hatchell, J., Fuller, G. A., & Richer, J. S. 2007, *Astronomy and Astrophysics*, 472, 187
- Heyer, M. H., Brunt, C., Snell, R. L., Howe, J. E., Schloerb, F. P., & Carpenter, J. M. 1998, *ApJS*, 115, 241
- Karr, J. L. & Martin, P. G. 2003, *Astrophysical Journal*, 595, 900
- Klein, R. I., Sandford, II, M. T., & Whitaker, R. W. 1983, *ApJ*, 271, L69
- Koenig, X. P., Allen, L. E., Gutermuth, R. A., Hora, J. L., Brunt, C. M., & Muzerolle, J. 2008, *Astrophysical Journal*, 688, 1142
- Lada, C. J. & Fich, M. 1996, *ApJ*, 459, 638
- Lefloch, B., Lazareff, B., & Castets, A. 1997, *Astronomy and Astrophysics*, 324, 249
- Muenter, J. 1975, *Journal of Molecular Spectroscopy*, 55, 490, is always cited for $\mu = 0.122$ debye.
- Oey, M. S., Watson, A. M., Kern, K., & Walth, G. L. 2005, *Astronomical Journal*, 129, 393
- Peters, T., Banerjee, R., Klessen, R. S., Low, M. M., Galvn-Madrid, R., & Keto, E. R. 2010, *The Astrophysical Journal*, 711, 1017
- Reipurth, B. & Bally, J. 2001, *Annual Review of Astronomy and Astrophysics*, 39, 403
- Shu, F. H., Adams, F. C., & Lizano, S. 1987, *ARA&A*, 25, 23
- Stanke, T., McCaughrean, M. J., & Zinnecker, H. 1999, *A&A*, 350, L43
- Taylor, A. R. et al. 2003, *AJ*, 125, 3145
- Thompson, M. A., White, G. J., Morgan, L. K., Miao, J., Fridlund, C. V. M., & Huldtgren-White, M. 2004, *Astronomy and Astrophysics*, 414, 1017
- Wilson, T. L., Rohlfs, K., & Hüttemeister, S. 2009, *Tools of radio astronomy* (Springer)

Table 2. CO 3-2 Outflows

Outflow Number	Latitude	Longitude	Velocity center (km s ⁻¹)	Velocity min	Velocity max	Mass (M_{\odot})	Momentum (M_{\odot} km s ⁻¹)	Energy (10 ⁴² ergs)	Dynamical Age (10 ⁴ years)	Momentum Flux $10^{-6} M_{\odot}$ km s ⁻¹ yr ⁻¹
1b	136.4437	1.2622	-35.5	-47.6	-40.3	0.034	0.26	21.1	7.0	7.2
1r	136.4674	1.2705	-35.5	-31.9	-23.4	0.04	0.24	17.3	7.0	7.2
2b	136.4899	1.1904	-35.5	-48.0	-39.7	0.011	0.07	4.9	5.4	4.4
2r	136.4743	1.2042	-35.5	-31.7	-23.0	0.025	0.17	13.0	5.4	4.4
3	136.475	1.2548	-31.8	-31.8	-26.8	0.025	0.12	5.8	-	-
4b	136.5086	1.2622	-36.4	-44.1	-40.1	0.011	0.07	4.2	6.5	1.7
4r	136.5109	1.2751	-36.4	-32.4	-28.6	0.011	0.04	1.8	6.5	1.7
5r	136.5113	1.2454	-35.3	-31.4	-28.8	0.009	0.04	1.9	4.9	3.7
5b	136.5236	1.2524	-35.3	-45.0	-39.2	0.025	0.14	8.0	4.9	3.7
6b	136.532	1.228	-34.4	-44.8	-40.0	0.007	0.04	3.0	1.5	8.8
6r	136.5321	1.2328	-34.4	-30.6	-24.0	0.012	0.09	6.6	1.5	8.8
7b	136.5449	1.2327	-35.1	-47.5	-39.9	0.018	0.13	10.4	2.2	12.1
7r	136.5498	1.2386	-35.1	-29.9	-22.7	0.018	0.13	9.9	2.2	12.1
8b	136.5795	1.2745	-32.7	-41.5	-39.3	0.004	0.02	1.0	4.6	6.3
8r	136.581	1.2601	-32.7	-30.0	-23.9	0.045	0.27	16.7	4.6	6.3
9b	136.67	1.2123	-35.6	-44.5	-38.5	0.025	0.13	7.2	3.9	4.2
9r	136.6766	1.2059	-35.6	-31.6	-26.7	0.009	0.04	1.8	3.9	4.2
10b	136.7172	0.7859	-42.9	-52.6	-47.5	0.068	0.41	25.7	3.9	22.0
10r	136.7271	0.7797	-42.9	-38.1	-33.1	0.074	0.45	28.0	3.9	22.0
11b	136.8195	1.082	-30.6	-40.7	-37.0	0.042	0.7	119.0	1.0	81.2
11r	136.8173	1.0799	-30.6	-31.4	-20.4	0.017	0.13	10.6	1.0	81.2
12b	136.8414	1.1512	-41.7	-53.3	-46.2	0.026	0.14	8.7	1.8	15.2
12r	136.8479	1.1517	-41.7	-34.6	-30.1	0.014	0.13	12.7	1.8	15.2
13	136.8461	0.8426	-31.0	-31.0	-23.5	0.016	0.05	1.9	-	-
14	136.8591	1.176	-54.5	-54.5	-47.1	0.01	0.06	4.1	-	-
15	136.9443	1.0841	-55.0	-55.0	-45.0	0.036	0.23	16.5	-	-
16b	137.3922	0.5964	-41.1	-47.0	-42.6	0.007	0.03	1.3	12.1	0.6
16r	137.3965	0.6125	-41.1	-38.7	-35.2	0.016	0.04	1.2	12.1	0.6
17b	137.4087	0.6761	-44.1	-57.9	-43.0	0.017	0.04	1.2	0.7	19.6
17r	137.4117	0.6755	-44.1	-37.6	-30.4	0.01	0.09	8.6	0.7	19.6
18b	137.4925	0.6289	-35.1	-39.2	-37.6	0.006	0.02	0.5	1.6	3.3
18r	137.4905	0.629	-35.1	-33.4	-31.0	0.013	0.03	1.0	1.6	3.3
19b	137.4815	0.6409	-33.9	-41.9	-38.9	0.011	0.05	2.4	0.7	9.6
19r	137.4798	0.6404	-33.9	-33.1	-25.9	0.005	0.01	0.2	0.7	9.6
20r	137.5356	1.279	-37.4	-33.0	-22.5	0.065	0.55	50.9	0.8	97.9
20b	137.5382	1.2786	-37.4	-49.2	-41.8	0.038	0.24	16.2	0.8	97.9
21b	137.6139	1.3533	-41.0	-52.0	-43.7	0.087	0.59	42.0	3.3	21.1
21r	137.6193	1.3603	-41.0	-35.2	-30.0	0.019	0.1	5.3	3.3	21.1
22	137.6215	1.5045	-46.0	-46.0	-40.3	0.026	0.08	3.1	-	-
23b	137.6389	1.5251	-37.2	-42.5	-40.5	0.011	0.03	0.9	4.5	1.3
23r	137.6449	1.5194	-37.2	-36.5	-32.0	0.01	0.03	1.0	4.5	1.3
24r	137.7094	1.4824	-38.2	-33.8	-25.4	0.037	0.3	26.1	1.7	34.1
24b	137.7146	1.4809	-38.2	-50.0	-42.7	0.047	0.28	18.3	1.7	34.1
25b	138.1403	1.6841	-38.5	-49.5	-43.2	0.014	0.1	7.0	1.4	32.1
25r	138.142	1.6884	-38.5	-34.3	-27.5	0.056	0.35	23.0	1.4	32.1
26b	138.2913	1.5538	-36.0	-52.0	-47.4	0.023	0.24	26.1	1.1	98.3
26r	138.2966	1.5564	-36.0	-30.0	-20.0	0.072	0.85	106.0	1.1	98.3
27	138.3017	1.5689	-30.0	-30.0	-22.0	0.026	0.3	36.0	-	-
28	138.3042	1.5437	-46.1	-46.1	-43.3	0.012	0.07	4.0	-	-
29	138.3053	1.5537	-51.6	-51.6	-45.3	0.024	0.45	85.3	-	-
30	138.3115	1.5443	-33.0	-33.0	-29.2	0.018	0.09	4.8	-	-
31	138.3184	1.5566	-49.1	-49.1	-44.4	0.016	0.09	5.1	-	-
32	138.3213	1.5658	-31.7	-31.7	-27.0	0.023	0.3	40.2	-	-
33b	138.3622	1.5048	-37.6	-49.5	-44.0	0.026	0.17	11.9	2.3	15.7
33r	138.3642	1.4959	-37.6	-34.7	-25.8	0.026	0.2	16.1	2.3	15.7
34r	138.4779	1.6137	-36.9	-33.1	-29.1	0.005	0.03	1.7	0.1	51.4
34b	138.478	1.6139	-36.9	-43.6	-40.6	0.007	0.03	1.2	0.1	51.4
35r	138.4998	1.6496	-37.5	-31.3	-24.1	0.013	0.12	11.6	1.3	18.7
35b	138.5021	1.6458	-37.5	-49.5	-43.6	0.014	0.12	11.0	1.3	18.7
36b	138.5034	1.6654	-38.5	-50.4	-42.3	0.025	0.19	15.8	2.7	10.7
36r	138.5061	1.6576	-38.5	-32.6	-26.7	0.014	0.1	6.8	2.7	10.7
37r	138.5208	1.6618	-38.5	-33.5	-31.4	0.008	0.04	1.6	2.2	5.1
37b	138.526	1.6651	-38.5	-47.0	-43.6	0.01	0.08	5.9	2.2	5.1
38b	137.498	0.6056	-35.9	-39.2	-38.5	0.004	0.01	0.4	0.2	8.5

APPENDIX A: OPTICALLY THIN, LTE DIPOLE MOLECULE

While many authors have solved the problem of converting CO 1-0 beam temperatures to H₂ column densities (Garden et al. 1991; Bourke et al. 1997; Cabrit & Bertout 1990; Lada & Fich 1996), there are no examples in the literature of a full derivation of the LTE, optically thin CO-to-H₂ conversion process. We present the full derivation here, and quantify the systematic errors generated by various assumptions.

We begin with the assumption of an optically thin cloud such that the radiative transfer equation (Wilson et al. 2009, eqn 1.9) simplifies to

$$\frac{dI_\nu}{ds} = -\kappa_\nu I_\nu \quad (\text{A1})$$

The absorption and stimulated emission terms yield

$$\kappa_\nu = \frac{h\nu_{ul}B_{ul}n_u}{c}\varphi(\nu) - \frac{h\nu_{ul}B_{lu}n_l}{c}\varphi(\nu) \quad (\text{A2})$$

where $\varphi(\nu)$ is the line shape function ($\int \varphi(\nu)d\nu \equiv 1$), n is the density in the given state, ν is the frequency of the transition, B is the Einstein B coefficient, and h is Planck's constant.

By assuming LTE (the Boltzmann distribution) and using Kirchoff's Law and the definition of the Einstein A and B values, we can derive a more useful version of this equation

$$\kappa_\nu = \frac{c^2}{8\pi\nu_{ul}^2}n_uA_{ul}\left[\exp\left(\frac{h\nu_{ul}}{k_B T_{ex}}\right) - 1\right]\varphi(\nu) \quad (\text{A3})$$

where k_B is Boltzmann's constant.

The observable T_B can be related to the optical depth, which is given by

$$\int \tau_\nu d\nu = \frac{c^2}{8\pi\nu_{ul}^2}A_{ul}\left[\exp\left(\frac{h\nu_{ul}}{k_B T_{ex}}\right) - 1\right] \int \varphi(\nu)d\nu \int n_u ds \quad (\text{A4})$$

Rearranging and converting from density to column ($\int nds = N$) gives an equation for the column density of the molecule in the upper energy state of the transition:

$$N_u = \frac{8\pi\nu_{ul}^2}{c^2 A_{ul}} \left[\exp\left(\frac{h\nu_{ul}}{k_B T_{ex}}\right) - 1\right]^{-1} \int \tau_\nu d\nu \quad (\text{A5})$$

In order to relate the brightness temperature to the optical depth, at CO transition frequencies the full blackbody formula must be used and the CMB must also be taken into account. Wilson et al. (2009) equation 15.29

$$T_B(\nu) = \frac{h\nu}{k_B} \left(\left[e^{h\nu/k_B T_{ex}} - 1 \right]^{-1} - \left[e^{h\nu/k_B T_{CMB}} - 1 \right]^{-1} \right) (1 - e^{-\tau_\nu}) \quad (\text{A6})$$

is rearranged to solve for τ_ν :

$$\tau_\nu = -\ln \left[1 - \frac{k_B T_B}{h\nu} \left(\left[e^{h\nu/k_B T_{ex}} - 1 \right]^{-1} - \left[e^{h\nu/k_B T_{CMB}} - 1 \right]^{-1} \right)^{-1} \right] \quad (\text{A7})$$

We convert from frequency to velocity units with $d\nu = \frac{\nu}{c}dv$, and plug (A7) into (A5) to get

$$N_u = \frac{8\pi\nu_{ul}^3}{c^3 A_{ul}} \left[\exp\left(\frac{h\nu_{ul}}{k_B T_{ex}}\right) - 1\right]^{-1} \int -\ln \left[1 - \frac{k_B T_B}{h\nu_{ul}} \left(\left[e^{h\nu_{ul}/k_B T_{ex}} - 1 \right]^{-1} - \left[e^{h\nu_{ul}/k_B T_{CMB}} - 1 \right]^{-1} \right)^{-1} \right] dv \quad (\text{A8})$$

which is the full LTE upper-level column density with no approximations applied.

The first term of the Taylor expansion is appropriate for $\tau \ll 1$ ($\ln[1+x] \approx x - \frac{x^2}{2} + \frac{x^3}{3} \dots$)

$$N_u = \frac{8\pi\nu_{ul}^3}{c^3 A_{ul}} \left[\exp\left(\frac{h\nu_{ul}}{k_B T_{ex}}\right) - 1\right]^{-1} \int \frac{k_B T_B}{h\nu_{ul}} \left(\left[e^{h\nu_{ul}/k_B T_{ex}} - 1 \right]^{-1} - \left[e^{h\nu_{ul}/k_B T_{CMB}} - 1 \right]^{-1} \right)^{-1} dv \quad (\text{A9})$$

which simplifies to

$$N_u = \frac{8\pi\nu_{ul}^2 k_B}{c^3 A_{ul} h} \frac{e^{h\nu_{ul}/k_B T_{CMB}} - 1}{e^{h\nu_{ul}/k_B T_{CMB}} - e^{h\nu_{ul}/k_B T_{ex}}} \int T_B dv \quad (\text{A10})$$

This can be converted to use μ_e (0.1222 for ¹²CO; Muenter 1975), the electric dipole moment of the molecule, instead of A_{ul} , using Wilson et al. (2009) equation 15.20 ($A_{ul} = \frac{64\pi^4}{3hc^3} \nu^3 \mu_e^2$):

$$N_u = \frac{3}{8\pi^3 \mu_e^2} \frac{k_B}{\nu_{ul}} \frac{2J_u + 1}{J_u} \frac{e^{h\nu_{ul}/k_B T_{CMB}} - 1}{e^{h\nu_{ul}/k_B T_{CMB}} - e^{h\nu_{ul}/k_B T_{ex}}} \int T_B dv \quad (\text{A11})$$

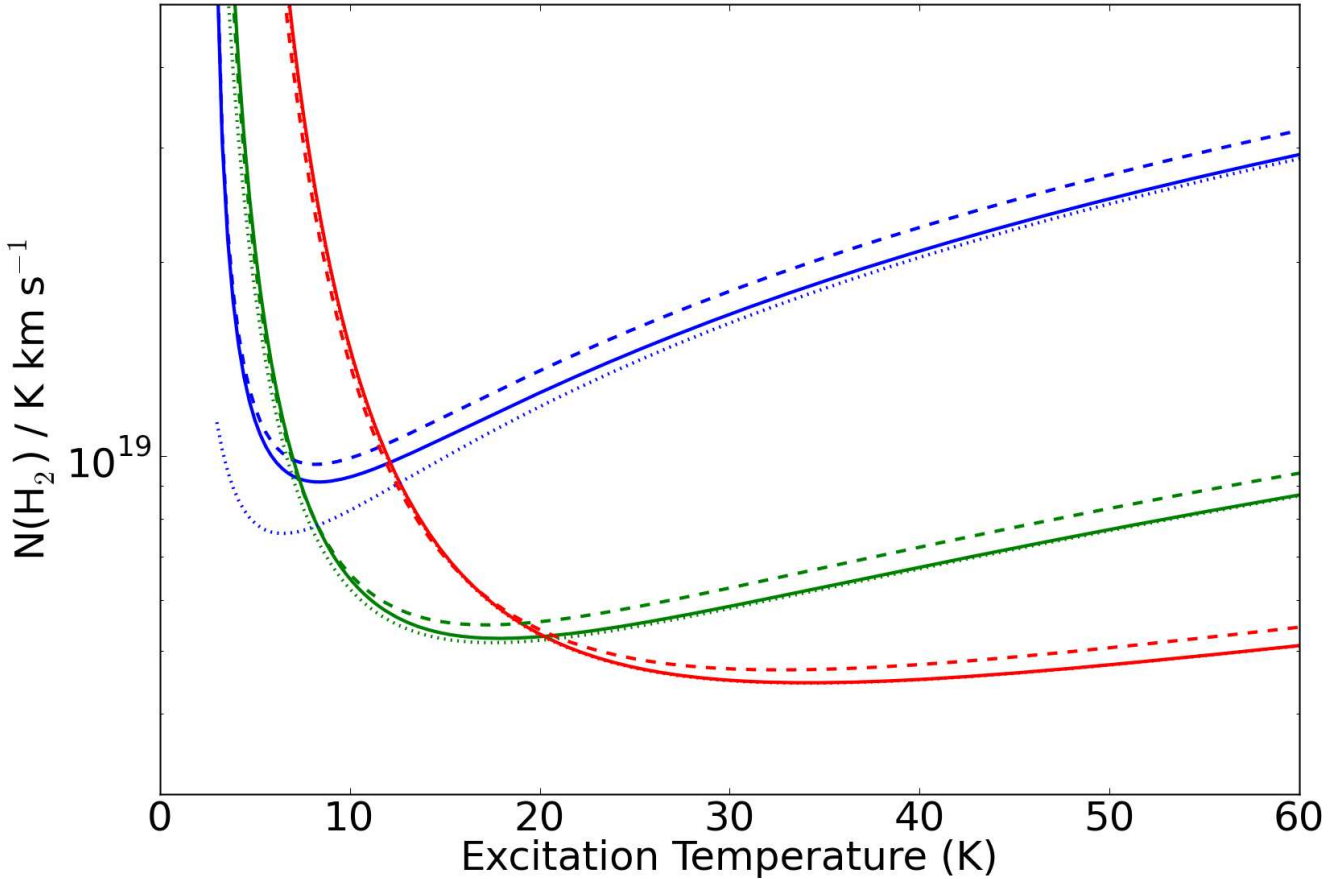


Figure A1. The LTE, optically thin conversion factor from T_B (K km s^{-1}) to $N(\text{H}_2)$ (cm^{-2}) assuming $X_{^{12}\text{CO}} = 10^{-4}$ plotted against T_{ex} . The dashed line shows the effect of using the integral approximation of the partition function (e.g. Cabrit & Bertout 1990). It is clearly a better approximation at low T_{ex} and is marginally, but systematically, offset for higher T_{ex} . The dotted line shows the effects of removing the CMB term from (A6); the CMB populates the lowest two excited states, but contributes nearly nothing to the $J = 3$ state. Top (blue): $J=1-0$, Middle (green): $J=2-1$, Bottom (red): $J=3-2$.

The total column can be derived from the column in the upper state using the partition function and the Boltzmann distribution

$$n_{tot} = \sum_{J=0}^{\infty} n_J = n_0 \sum_{J=0}^{\infty} (2J+1) \exp\left(-\frac{J(J+1)B_e h}{k_B T_{ex}}\right) \quad (\text{A12})$$

(A13)

This equation is frequently approximated using an integral (e.g. Cabrit & Bertout 1990), but a more accurate numerical solution using up to thousands of rotational states is easily computed

$$n_J = \left[\sum_{j=0}^{j=j_{max}} (2j+1) \exp\left(-\frac{j(j+1)B_e h}{k_B T_{ex}}\right) \right] (2J+1) \exp\left(-\frac{J(J+1)B_e h}{k_B T_{ex}}\right) \quad (\text{A14})$$

The effects of using the approximation and the full numerical solution are shown in figure A1.

The CO 3-2 transition is also less likely to be in LTE than the 1-0 transition. The critical density ($n_{cr} \equiv A_{ul}/C_{ul}$) of ^{12}CO 3-2 is 27 times higher than that for 1-0. We have run RADEX LVG models of CO to examine the impact of sub-thermal excitation on column derivation. The results of the RADEX models are shown in Figure A2. They illustrate that, while it is quite safe to assume the CO 1-0 transition is in LTE in most circumstances, a similar assumption is probably invalid for the CO 3-2 transition in typical molecular cloud environments.

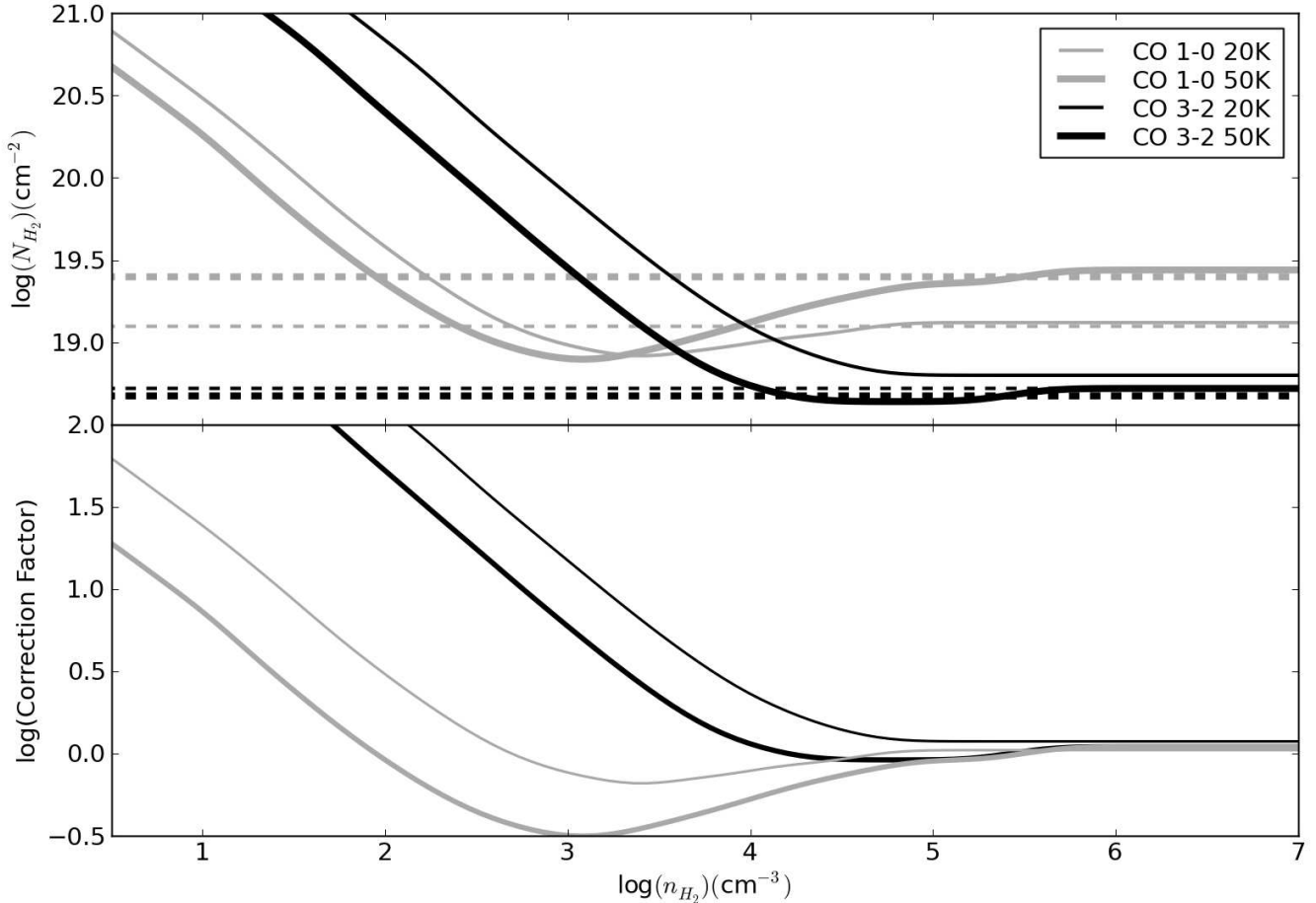


Figure A2. Top: The derived $N(H_2)$ as a function of n_{H_2} for $T_B = 1$ K. The dashed lines represent the LTE-derived $N(H_2)/T_B$ factor, which has no density dependence and, for CO 3-2, only a weak dependence on temperature. Bottom: The correction factor ($N(H_2)_{RADEX} / N(H_2)_{LTE}$) as a function of n_{H_2} . For $T_K = 20$ K, the “correction factor” at 10^3 cm^{-3} (typical GMC densities) is ~ 15 , while at 10^4 cm^{-3} (closer to n_{crit} but perhaps substantially higher than GMC densities) it becomes negligible. The correction factor is also systematically lower for a higher gas kinetic temperature. For some densities, the “correction factor” dips below 1, particularly for CO 1-0. This effect is from a slight population inversion due to fast spontaneous decay rates from the higher levels and has been noted before (e.g. Goldsmith 1972).